

Episodic mass loss in the very luminous red supergiant [W60] B90 in the Large Magellanic Cloud

G. Munoz-Sanchez^{1,2}, S. de Wit^{1,2}, A.Z. Bonanos¹, K. Antoniadis^{1,2}, K. Boutsia^{4,5},
P. Boumis¹, E. Christodoulou^{1,2}, M. Kalitsounaki^{1,2}, and A. Udalski⁶

¹ IAASARS, National Observatory of Athens, Metaxa & Vas. Pavlou St., 15236, Penteli, Athens, Greece

² Department of Physics, National and Kapodistrian University of Athens, Panepistimiopolis, Zografos, 15784, Greece

³ Institute of Astrophysics, FORTH, GR-71110, Heraklion, Greece

⁴ Mid-Scale Observatories/NSF NOIRLab, 950 N. Cherry Ave., Tucson, AZ 85719, USA

⁵ Las Campanas Observatory, Carnegie Observatories, Colina El Pino, Casilla 601, La Serena, Chile

⁶ Astronomical Observatory, University of Warsaw, Al. Ujazdowskie 4, 00-478 Warsaw, Poland

ABSTRACT

Context. Despite mounting evidence that extreme red supergiants (RSGs) undergo episodic mass loss events, their role in RSG evolution remains uncertain. Critical questions, such as whether these events can strip the star, and what is their timescale and frequency, remain unanswered.

Aims. This study delves into [W60] B90, one of the most luminous and extreme RSGs in the Large Magellanic Cloud (LMC), aiming to search for evidence of episodic mass loss. Our discovery of a bar-like nebular structure at 1 pc, reminiscent of the bar around Betelgeuse, raised the question of whether [W60] B90 also has a bow shock and, thus, motivated our study.

Methods. We collected and analyzed proper motion data from *Gaia*, as well as new multi-epoch spectroscopic and imaging data, and archival time-series photometry in the optical and mid-infrared. We used MARCS models to derive the physical properties of the star from the spectra.

Results. We found [W60] B90 to be a walkaway star, with a supersonic peculiar velocity in the direction of the bar. We detected shocked emission between the bar and the star, based on the $[S\ II]/H\alpha > 0.4$ criterion, providing strong evidence for a bow shock. The 30 yr optical light curve revealed semi-regular variability, showing three similar dimming events with $\Delta V \sim 1$ mag, a recurrence of ~ 12 yr, and a rise time of 400 days. We found the mid-IR light curve to vary by 0.51 mag and 0.37 mag in the WISE1 and WISE2 bands, respectively, and by 0.42 mag and 0.25 mag during the last dimming event. During this event, optical spectroscopy revealed spectral variability (M3 I to M4 I), a correlation between the T_{eff} and the brightness, increased extinction, and, after the minimum, spectral features incompatible with the models. We also found a difference of >300 K between the T_{eff} measured from the TiO bands in the optical and the atomic lines from our *J*-band spectroscopy.

Conclusions. [W60] B90 is a more massive analog of Betelgeuse in the LMC and therefore the first extragalactic single RSG with a suspected bow shock. Its high luminosity $\log(L/L_{\odot}) = 5.32$ dex, mass-loss rate, and mid-IR variability compared to other RSGs in the LMC, indicate that it is in an unstable evolutionary state undergoing episodes of mass loss. Investigating other luminous and extreme RSGs in low-metallicity environments using both archival photometry and spectroscopy is crucial to understanding the mechanism driving episodic mass loss in extreme RSGs in light of the Humphreys-Davidson limit and the “RSG problem”.

Key words. Stars: individual: [W60] B90, stars: massive - stars: supergiants - stars: atmospheres - stars: late-type - stars: mass-loss

1. Introduction

Red supergiants (RSGs) are evolved massive stars with initial masses between 8 – 25 M_{\odot} (Ekström et al. 2012; Levesque 2017). During their evolution, RSGs increase their luminosity and therefore manifest larger radii and cooler temperatures, before ending their life by exploding as a supernova (SN) or collapsing directly into a black hole (Smartt 2015; Sukhbold et al. 2016; Adams et al. 2017; Laplace et al. 2020). Despite only spending 10% of its time as RSGs, the most mass is lost during this phase of the evolution. Empirical relations have revealed a robust correlation between luminosity and mass loss within the RSG phase (e.g. de Jager et al. 1988; van Loon et al. 2005). RSGs are more prone to exhibiting spectral type variability as they become more luminous and cooler (Levesque et al. 2007; Dorda & Patrick 2021), but the mechanisms responsible for these phenomena remain unknown. Evidence for episodic mass ejections has been found around extreme RSGs

(e.g. VY CMa or Betelgeuse; Decin et al. 2006; Dupree et al. 2022), but the relevance of these events is still unclear. Recently, Betelgeuse surprised the community when it unexpectedly decreased in brightness. This ‘Great Dimming’ was explained by a multi-wavelength follow-up to be the result of a mass ejection that formed dust and obscured the star (Montargès et al. 2021; Drevon et al. 2024). Montargès et al. (2021) determined the ejected mass to be between 3 – 120% of the annual mass lost by Betelgeuse, demonstrating that the significance of episodic mass loss is uncertain by two orders of magnitude.

Despite being one of the brightest stars in the sky, Betelgeuse exhibits many properties that remain unexplained (see e.g. Wheeler & Chatzopoulos 2023). The bow shock and bar structure in the vicinity of the star are particularly unusual (Noriega-Crespo et al. 1997a). The origin of the bar is uncertain, as some arguments support the relation to Betelgeuse (Mackey et al. 2012), while others advocate for an interstellar origin (Decin et al. 2012; Meyer et al. 2021). Contrarily, the physics behind the

bow shock is well understood as it is produced when a star moves supersonically and the stellar wind interacts with the interstellar medium (ISM), creating an arc-like shape. Although they are commonly seen in OB runaways (Noriega-Crespo et al. 1997b), only two other cases of Galactic single RSGs are known: μ Cep and IRC-10414 (Cox et al. 2012; Gvaramadze et al. 2014). Their detection is useful to constrain the properties of the local ISM and the stellar wind (Hollis et al. 1992; Kaper et al. 1997). Due to the lack of a sophisticated grid of RSG models including the wind, deriving the mass-loss rate, \dot{M} , directly from optical spectroscopy is still impossible. Instead, the \dot{M} of RSGs is commonly derived from the mid-IR excess of the spectral energy distribution (SED) (e.g. Riebel et al. 2012; Yang et al. 2023; Antoniadis et al. 2024). However, it depends on general assumptions such as the gas-to-dust ratio, dust grain size, and mechanism of the wind, which introduce large uncertainties in the results. Therefore, the bow shock in RSGs provides a unique and independent scheme to estimate the \dot{M} and compare with the other methods.

[W60] B90 is one of the most luminous RSGs in the Large Magellanic Cloud (LMC). It was reported by de Wit et al. (2023), within the ASSESS project (Bonanos et al. 2023, Episodic mAss loSS in Evolved maSSive Stars), to have extreme parameters similar to WOH G64 (Levesque et al. 2009). Our discovery of a bar-like structure, similar to the bar of Betelgeuse, at 1 pc from the star in an archival *Hubble* Space Telescope (HST) image, immediately raised the question of whether [W60] B90 could be the first extragalactic RSG with a bow shock. Moreover, its high luminosity close to the observed upper limit of RSGs in the LMC ($\log(L/L_{\odot}) = 5.50$ dex; Davies et al. 2018) and its high mass-loss rate within the LMC ($\dot{M} = 5.07 \times 10^{-6} M_{\odot} \text{ yr}^{-1}$, Antoniadis et al. 2024), indicate that this RSG is in an evolved evolutionary state undergoing considerable mass loss.

In this paper, we present a detailed analysis of [W60] B90. We collected archival photometry to study the long-term photometric variability and we performed a multi-epoch spectroscopic campaign both to study its current spectral variability and search for evidence of shocked material in the circumstellar environment. In Sect. 2, we describe the observations obtained and the archival data used. In Sect. 3, we investigate the membership of [W60] B90 to the LMC and its relation to the bar. We analyze the spectroscopic data for the circumstellar nebular emission and examine its shocked origin. In Sect. 4 we analyze the light curve, the variability in the optical and the mid-IR, and present the results derived from our optical and near-IR spectroscopic observations. In Sect. 5 we discuss the results and evolutionary status of the star, while in Sect. 6, we summarize the conclusions.

2. Observations and data reduction

We discovered a nebular bar structure located at $4''$ from [W60] B90 on an HST image available in the Hubble Legacy Archive¹ (see Fig. 1). The observations were obtained on 2007-07-27 UT05:34:16, under the program ID 10583, with an exposure time of 1000s and the F675W filter. Below, we describe the archival photometry collected and our spectroscopic observations of [W60] B90.

2.1. Photometric catalogs

We assembled the light curve of [W60] B90 by compiling archival photometry² spanning ~ 30 yrs from the following sur-

veys: ATLAS forced photometry (Tonry et al. 2018; Heinze et al. 2018; Shingles et al. 2021), ASAS (Pojmanski 1997), ASAS-SN (Shappee et al. 2014; Kochanek et al. 2017), *Gaia* DR3 (*Gaia* Collaboration et al. 2016, 2023), the MACHO project (Alcock et al. 1997), NEOWISE (Mainzer et al. 2011), OGLE (Udalski et al. 1997, 2008, 2015), the *Spitzer* SAGE and SAGE-var projects (Meixner et al. 2006; Riebel et al. 2015), and *WISE* (Wright et al. 2010; Cutri et al. 2021). We applied the following criteria to each survey to select the most reliable data:

- ATLAS: we used forced photometry on reduced images to obtain the light curve from the server. We used data points with flag $err = 0$, $chi/N < 100$, and an error below 0.1 mag.
- ASAS: we used the photometry based on the smallest aperture (2 px) to avoid contamination from other sources due to the small pixel scale of the instrument ($16'' \text{ px}^{-1}$). We used the mean data, (i.e. *B* flag-category) to obtain a cleaner light curve.
- ASAS-SN: we retrieved the data from Sky Patrol, selecting the *image subtraction with reference flux added* option as it uses co-added data, considerably decreasing the photometry error. We rejected epoch photometry with errors above 0.1 mag, and removed the *bm* camera data in the *g*-band, due to a systematic offset in the flux with respect to the other cameras.
- MACHO: we only used the V_{KC} -band as the star saturates in the I_{KC} -band. The MACHO calibration uses the $V_{KC} - I_{KC}$ color (see Eq. 1 and 2 in Alcock et al. 1999), hence we computed the V_{KC} -band considering the approximation $V_{KC} \approx V_{M,i} + a_0 + 2.5 \log(ET)$, where a_0 is the zero-point coefficient and ET is the exposure time. We applied a 3σ clipping to discard outliers with small errors.
- NEOWISE: [W60] B90 has been observed since the mission started in 2014 during 20 epochs, each lasting over one week. We binned all the photometric measurements within an epoch by taking the median value and the uncertainty of the median. We discarded data with $qual_frame = 0$ and $chi^2 > 20$. However, NEOWISE photometry differs from ALLWISE for targets brighter than $W1 < 8$ mag and $W2 < 7$ mag. Hence, we applied an offset according to Fig. 6 in Mainzer et al. (2014) to correct the magnitudes.
- OGLE: we used *I*-band data from the OGLE-III shallow survey (Ulaczyk et al. 2013), and *V*-band data from the OGLE-II, OGLE-III, and OGLE-IV databases. Unfortunately, the star is saturated in the images of the main *I*-band monitoring of the LMC by OGLE, conducted continuously over the last 27 years.
- *Spitzer*: we collected the epoch photometry from the SAGE and SAGE-var projects.

2.2. Optical spectroscopy

We performed spectroscopic observations with the Magellan Echellette (MagE) spectrograph (Marshall et al. 2008) placed on the 6.5-m Baade telescope at Las Campanas Observatory, Chile. We used the $0.7'' \times 10''$ long-slit, providing a wavelength coverage of 3500 – 9500Å, a spectral resolution of $R \sim 5000$, and a spatial resolution of $0.3'' \text{ px}^{-1}$ with binning 1×1 . Table 1 shows the coordinates of the slit center, UT date of the observations, the instrument, the exposure time, the position angle (PA) of the slits, and the slit width. The slits labeled Epoch1-Epoch4 were centered on the RSG, while slits Neb1-Neb6 were placed around the star to search for shocked material. We used the MagE pipeline (Kelson et al. 2000; Kelson 2003) for the

¹ <https://hla.stsci.edu/>

² Updated up to the submission date of the paper.

bias and flat correction. We continued the reduction based on the ECHELLE package of IRAF³, as we detected small artifacts in later steps of the MagE pipeline that could compromise the nebular emission. Finally, we used a flux standard to calibrate in flux the spectra with the IRAF routines STANDARD and SENSFUNC.

We divided each slit into small sections to investigate the spatial distribution of the nebular emission. We extracted several apertures of 3 px (0.9'' or ~ 0.25 pc for the distance of the LMC) in areas of the slits without contamination from background sources (see Table B.1). We consider the 3 px aperture optimal as it minimizes the stellar contamination, achieves a better spatial resolution of the analysis of the circumstellar material (CSM), provides an adequate S/N, and avoids a large impact from artifacts. The slits labeled Epoch1 and Neb1-3 did not have acquisition images. We obtained their position and orientation using the header parameters instead.

2.3. Near-IR spectroscopy

We observed [W60] B90 with the Folded-port InfraRed Echelle (FIRE) instrument placed on the 6.5-m Baade telescope at Las Campanas Observatory, Chile, on January 30, 2021 (Table 1). Using the 0.6'' slit and the binning 1 \times 1, we covered the range 0.84 – 2.4 μm with a spectral resolution of $R \sim 6000$ and pixel scale of 0.15'' px⁻¹. We obtained four exposures of 15 seconds with the high-gain mode following an ABBA pattern. We reduced the data with the official FIRE pipeline developed in IDL⁴, including the telluric correction and the flux calibration of the spectra.

2.4. Spitzer spectroscopy

[W60] B90 was observed spectroscopically by *Spitzer* with the IRS instrument (Houck et al. 2004) inside the programs ID1094 (AORKEY: 6076928) and ID40061 (AORKEY: 22272512). Four modules were used (Short-Low, Short-High, Long-Low, and Long-High) covering the spectral region from 5.2 μm to 38 μm and providing low ($R \sim 60 - 130$) and high ($R \sim 600$) resolution for the short and long configurations. However, we used only the Short-Low of Program ID1094 from Level 2 of the Post Basic Calibrated Data (PBCD) because an unidentified nearby source contaminated the longer wavelengths. This source is comparable in brightness to [W60] B90 only in MIPS1 (24 μm) images. The data from program ID40061 were discarded, as the star was not properly centered on the slit on the short-low exposures. Finally, we added the synthetic photometry at 12 and 16 μm provided in the IRS table to include them in the SED fitting (see sect. 5.6).

3. Evidence of shocked material

3.1. LMC membership and proper motion

Gaia DR3 reported a parallax 0.0457 ± 0.0270 mas for [W60] B90, which corresponds to a distance of 22^{+32}_{-8} kpc. This uncertainty prevented us from determining whether [W60] B90 belongs to the LMC or our Galaxy. de Wit et al. (2023) previously analyzed the membership to the LMC based on the radial velocity (RV) from Ca II triplet, its position within the LMC

³ IRAF is distributed by the National Optical Astronomy Observatory, operated by the Association of Universities for Research in Astronomy (AURA) under agreement with the National Science Foundation.

⁴ <https://wikis.mit.edu/confluence/display/FIRE/FIRE+Data+Reduction>

and *Gaia* DR2. We go one step further and use the kinematic analysis of the LMC by Jiménez-Arranz et al. (2023), based on *Gaia* DR3, which derived a probability P_{LMC} for stars within the field of the LMC to belong to that galaxy. They report $P_{LMC} = 0.87$ for [W60] B90, with $P_{LMC} = 0$ corresponding to a foreground star, $P_{LMC} = 1$ to a highly probable LMC member, and $P_{LMC} = 0.52$ as the class cut-off limit. Considering also the RVs of 263 km s⁻¹ reported by *Gaia* DR3, we conclude that [W60] B90 is a genuine LMC member.

Next, we investigated whether [W60] B90 and the bar are physically related. We computed the peculiar velocity of the RSG, to determine whether it moves in the direction of the bar. The motion towards the bar would be consistent with a bow shock scenario, where the interaction of the wind with the ISM causes shock-ionization. We used *Gaia* DR3 to collect the proper motions (PMs) of all the stars within a cone radius of 1.8' to 36' centered W60 B90. We then cleaned the sample from foreground contamination using Jiménez-Arranz et al. (2023), and obtained a median value of the PM within the cone. This value was then subtracted from the PM of [W60] B90 to obtain the local motion. Finally, we tested the robustness of our analysis by exploring different cone sizes and probability thresholds to clean the foreground contamination. We selected 36', 18', 6', 4.5', 3', 2.4', and 1.8' for the cone sizes, which correspond to local distances of 520, 260, 87, 65, 43, 35, and 26 pc, assuming a distance $D = 49.59$ kpc to the LMC (Pietrzyński et al. 2019). We considered the probability thresholds $P_{LMC} = 0.5, 0.7,$ and 0.9 . Table A.1 lists the derived proper motion and peculiar velocity of [W60] B90 as a function of the cone size and P_{LMC} . N_{Gaia} is the number of stars inside the cone, while N_{clean} is the number of stars remaining after the foreground cleaning.

We present the results for $P_{LMC} = 0.7$ in Fig. 1 as an example. Our analysis reveals that the selected P_{LMC} thresholds barely affect the results, while the direction of the peculiar velocity varies slightly, depending on the cone size. These variations are considerably smaller than the 1σ error from *Gaia* DR3, and all are consistent with the projected motion of the star towards the bar. We derived a peculiar velocity ranging from 16 – 25 (± 11) km s⁻¹ depending on the parameters assumed, but still compatible with moving faster than the speed of sound (see Sect. 5.1). Forthcoming *Gaia* releases are needed to improve the accuracy of the PM, reducing the uncertainties on the orientation and absolute value of the peculiar velocity of [W60] B90.

3.2. The [S II]/H α ratio

Nebular emission can arise from the energy released in shocks or photoionizing radiation depending on the physical conditions. Historically, the ratio [S II]/H α has been used to separate between the two mechanisms, being photoionized when [S II]/H $\alpha < 0.4$ and shocked when [S II]/H $\alpha \geq 0.4$ (Mathewson & Clarke 1973). In H II regions, the radiation from hot stars ionizes sulfur mainly to S III. However, when shocks cause nebular emission, the energy is insufficient to produce S III, and S II becomes the main state of sulfur, increasing the [S II]/H α ratio. Although some works have identified shocked material with ratios down to [S II]/H $\alpha = 0.3$ (Fig. 5 in Kopsacheili et al. 2020; Gvaramadze et al. 2014), we considered 0.4 to be a more conservative criterion to confirm the presence of shocked material.

We used the spectra presented in Table 1 to analyze the nebular emission of the CSM. We measured the flux and the error of the emission lines with the IRAF task SPLIT. We dereddened the fluxes using the Balmer decrement, which is the difference between the observed ratio of the intensities H α /H β with the the-

Table 1: Log of the long-slit observations with the 6.5-m Baade telescope

Slit name	RA (J2000)	Dec. (J2000)	UT Date	Instrument	Exp. time (s)	PA ^a (°)	Slit width (″)
Epoch1 ^b	05:24:19.31	-69:38:49.4	2020-03-08	MagE	3 × 180 + 1 × 240	60	1.0
EpochJ	05:24:19.31	-69:38:49.3	2021-01-30	FIRE	4 × 15	13	0.6
Epoch2	05:24:19.24	-69:38:50.2	2022-12-02	MagE	3 × 180 + 1 × 240	17	0.7
Epoch3	05:24:19.29	-69:38:49.4	2023-04-07	MagE	3 × 180 + 1 × 240	90	0.7
Epoch4	05:24:19.29	-69:38:49.7	2023-09-28	MagE	3 × 180	90	0.7
Neb1	05:24:20.22	-69:38:48.2	2022-03-20	MagE	3 × 400	77	0.7
Neb2	05:24:20.06	-69:38:48.1	2022-03-20	MagE	3 × 400	120	0.7
Neb3	05:24:20.00	-69:38:45.4	2022-03-20	MagE	3 × 400	79	0.7
Neb4	05:24:19.60	-69:38:47.0	2022-12-02	MagE	3 × 400	111	0.7
Neb5	05:24:20.00	-69:38:51.8	2022-12-02	MagE	3 × 400	9	0.7
Neb6	05:24:19.94	-69:38:45.0	2023-09-28	MagE	3 × 400	160	0.7

Notes. ^(a) The position angle PA = 0° refers to the South-to-North direction, while PA = 90° is the West-to-East direction.

^(b) From de Wit et al. (2023).

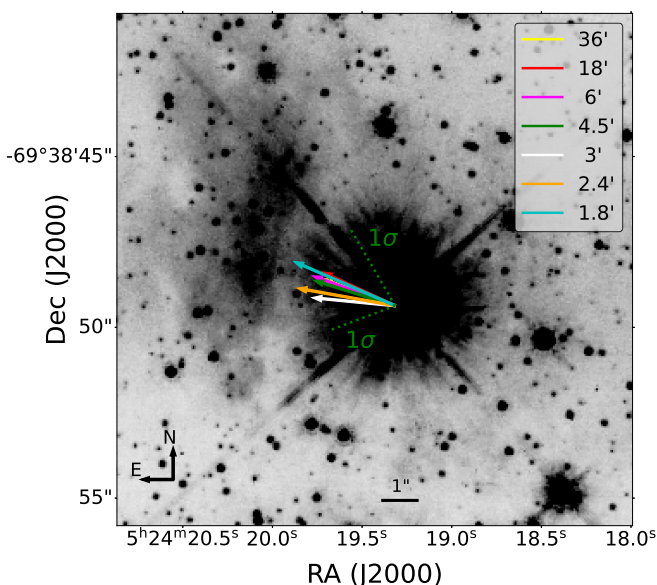


Fig. 1: HST F675W image of [W60] B90 showing the PM analysis for $P_{LMC} = 0.7$. The arrows represent the peculiar velocity direction of [W60] B90 for each cone to compute the local PM of the LMC. The length of the arrows is scaled with the peculiar velocity. The green dotted lines show the 1σ PM error from *Gaia* DR3 on the 4.5' cone size.

oretical ratio of 2.86 (assuming $T_e = 10^4$ K and $n_e = 100$ cm⁻³; Osterbrock 1989). We used the Python tool PyNeb (Luridiana et al. 2015) to calculate $E(B - V)$ and $c(H\beta)$ for each spectrum and dereddened them accordingly using the Gordon et al. (2003) extinction law for the LMC. We established a detection limit of 3σ to include a line in the analysis. We report the locations of each aperture extracted in Table B.1 and the measurements of the nebular emission in Table B.2. In the latter table, we show the identified lines, their central wavelength, the observed and dereddened fluxes relative to $H\beta$, the signal-to-noise ratio (S/N) of the line, the radial velocity, the extinction coefficients $E(B - V)$ and $c(H\beta)$, and the ratios of the ions.

We present the measured $[S\ II]/H\alpha$ ratios in the circumstellar environment of [W60] B90 in the left panel of Figure 2. The values $[S\ II]/H\alpha > 0.4$ (highlighted in green) indicate the presence of shocked material and are concentrated between the bar

and the star along the direction of the motion of the star (see Sect. 3.1), supporting the argument of the interaction of the star and the CSM in the direction of the bar. Contrarily, we measured the lowest ratios in areas opposite to the movement of the star and perpendicular to the direction of the motion. To show the variation of nebular emission among apertures, we show the highest and lowest $[S\ II]/H\alpha$ ratio in the upper right panel of Fig. 2. Moreover, we used the Epoch2 and Epoch3 slits, which were centered on the RSG and oriented in North-South and East-West directions, to examine the inhomogeneity of the CSM. To extract symmetric apertures at the North, South, East, and West positions, we took the peak of the emission as a reference from the trace of the star in the 2D images. We chose a distance of 7 px ($\sim 2.1''$) from the peak as it was a good compromise between being close to the star and not having the nebular emission embedded in the continuum of the RSG. We compare the four positions in the lower right panel of Fig. 2 to highlight the inhomogeneous emission at a distance of $2.1''$ (~ 0.5 pc) from [W60] B90.

3.3. Other line ratios

We used other line ratios to verify the origin of the nebular emission around [W60] B90, including the ratios $[O\ I]/H\alpha$, $[O\ II]/H\beta$, $[O\ III]/H\beta$, $[N\ II]/H\alpha$, and $[S\ II]/H\alpha$. In Fig. C.1, we compare our measurements with the diagnostics presented in Kopsacheili et al. (2020). The diagnostics for all the apertures agree with a shocked scenario, except for $[O\ III]$, which indicates a photoionized mechanism. This may be explained by the fact that the models in Kopsacheili et al. (2020) only apply to shocks with velocities between 100–1000 km s⁻¹, while the peculiar velocity of [W60] B90 is ≤ 35 km s⁻¹. Material ejected from the star at such a low velocity will not contain enough energy to ionize O II to O III. The presence of a nearby H II region at 14'' (LHA 120-N 132B; Henize 1956) and the newly discovered B1V star at 7'' (see Appendix D) could also explain the photoionized nature of $[O\ III]$. Radiation from nearby hot stars might contribute to the ionization of the gas around our RSG and cause the emission in areas with low $[S\ II]/H\alpha$. Even in the shocked areas, nebular emission might arise from a combination of shocks and photoionization from nearby hot stars. Another explanation for the inconsistency of $[O\ III]$ is the brightness of the line. In all the apertures, the strength of $[O\ III]\ \lambda 5007$ was approximately at the noise level (3σ detection), hence the fluxes might be underestimated, leading to lower ratios.

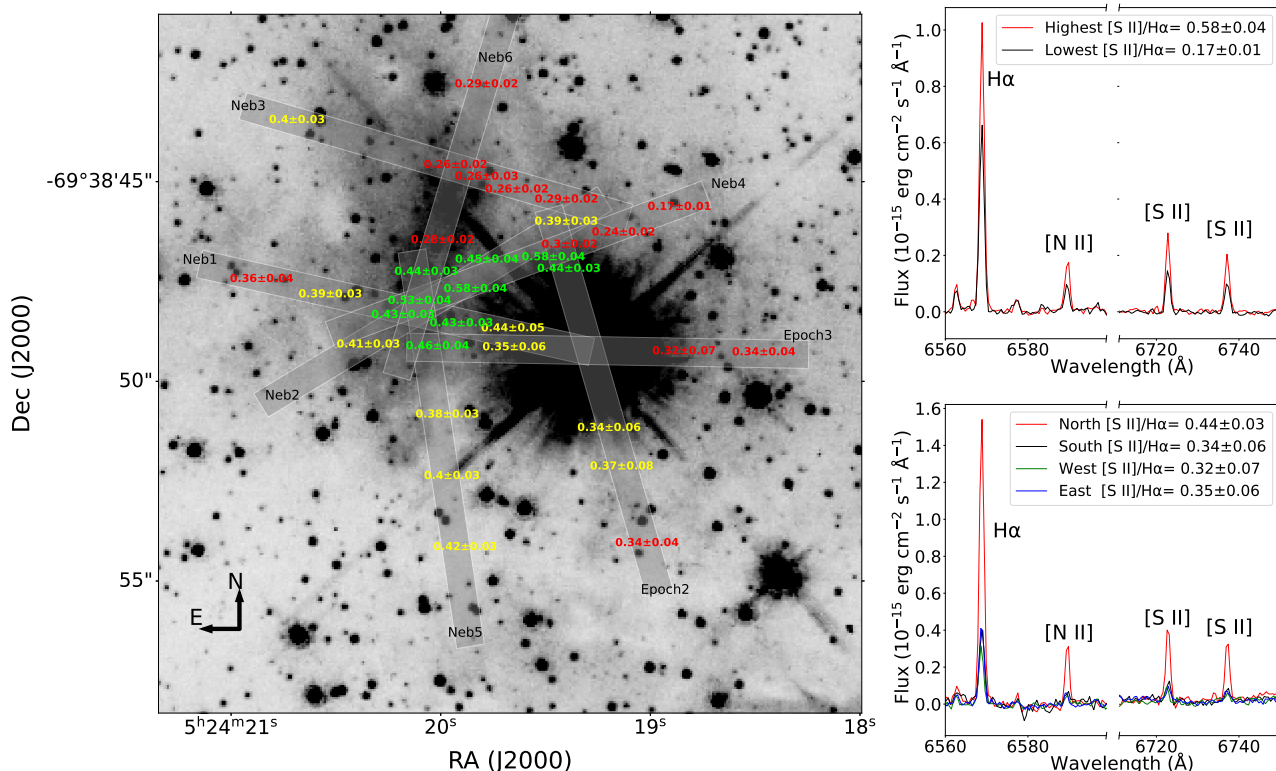


Fig. 2: *Left*: HST F675W image with the slits and the $[S\ II]/H\alpha$ ratio for each aperture overlaid. The green color corresponds to ratios above 0.4 within the error, the yellow color corresponds to ratios with a lower limit below 0.4, and the red color corresponds to apertures below 0.4 within the error. *Right*: Comparison of the emission lines between the apertures with the highest and the lowest $[S\ II]/H\alpha$ ratio (*top*) and the apertures 2.1'' North, South, East, and West of the star (*bottom*).

3.4. Radial velocity of the CSM

We measured the RV of the CSM from the central wavelengths of the Balmer lines and forbidden emission lines detected (see Table B.2). We compared the RV of each ion at every location observed around [W60] B90. However, the difference in the RV among the apertures was smaller than the $\pm 7\text{ km s}^{-1}$ error derived from the spectral resolution, preventing us from studying how the RVs are spatially distributed. We have, however, computed the median RV of each ion, using the individual velocities from each aperture (Table 2). We grouped the lines $[S\ II]\ \lambda\lambda 6717, 6731$ and $[O\ II]\ \lambda\lambda 3726, 3729$ to compute a single RV for $[S\ II]$ and $[O\ II]$, respectively. Given that the RV of [W60] B90 is $263.49 \pm 1.02\text{ km s}^{-1}$ from *Gaia* DR3, we compared the kinematics of the nebular material to the kinematics of the star. All nebular lines are redshifted by $\sim 10\text{ km s}^{-1}$ compared to the star, except $[S\ II]$ and $[O\ I]$ which are $\sim 20\text{ km s}^{-1}$ and $\sim 40\text{ km s}^{-1}$, respectively. Each estimate is consistent with the low-velocity scenario ($\leq 100\text{ km s}^{-1}$).

4. Variability of [W60] B90

4.1. Optical light curve

We assembled multi-epoch photometry of [W60] B90 from 1992 to the submission date of this work and we present the optical light curve in Fig. 3. We subtracted the mean value of each data set to obtain a relative magnitude, allowing for a comparison between different filters and surveys (see lower panel of Fig. 3). The amplitude of the ASAS-SN data is smaller than other surveys due to its pixel scale ($8''\text{px}^{-1}$). Nearby sources are blended

Table 2: Mean radial velocity of the CSM

Ion	RV (km s^{-1})	Ion	RV (km s^{-1})
$H\alpha$	275 ± 2	$[O\ I]$	310 ± 4
$H\beta$	276 ± 3	$[O\ II]$	272 ± 4
$[S\ II]$	284 ± 3	$[O\ III]$	276 ± 5
$[N\ II]$	277 ± 4		
[W60] B90		263.49 ± 1.02	

Notes. Spectral resolution error is $\pm 7\text{ km s}^{-1}$.

with [W60] B90, contaminating the data by adding a constant flux, which yields a lower amplitude. Nevertheless, we considered ASAS-SN as a guideline for the general shape of the light curve between 2017 and 2022, due to the lack of other data covering these years. After 2022, ATLAS and OGLE *V*-band provide better photometry due to their improved pixel scale (1.86 and $0.26''\text{px}^{-1}$, respectively).

We classify [W60] B90 as a semi-regular variable based on the short-period variability of $\Delta m < 0.5\text{ mag}$ (Kiss et al. 2006), improving on the previous classifications: long-period variable (LPV; *Gaia* Collaboration et al. 2023; Watson et al. 2006; Fraser et al. 2008) and non-periodic variable (Jayasinghe et al. 2018). However, three exceptional events stand out with $\Delta m \sim 1\text{ mag}$ and a rise time of $\sim 400\text{ d}$ (Fig. 4). We present a comparison of the *V*-band from AAVSO of the Great Dimming of Betelgeuse, the recent dimming of RW Cep (Anugu et al. 2023) and

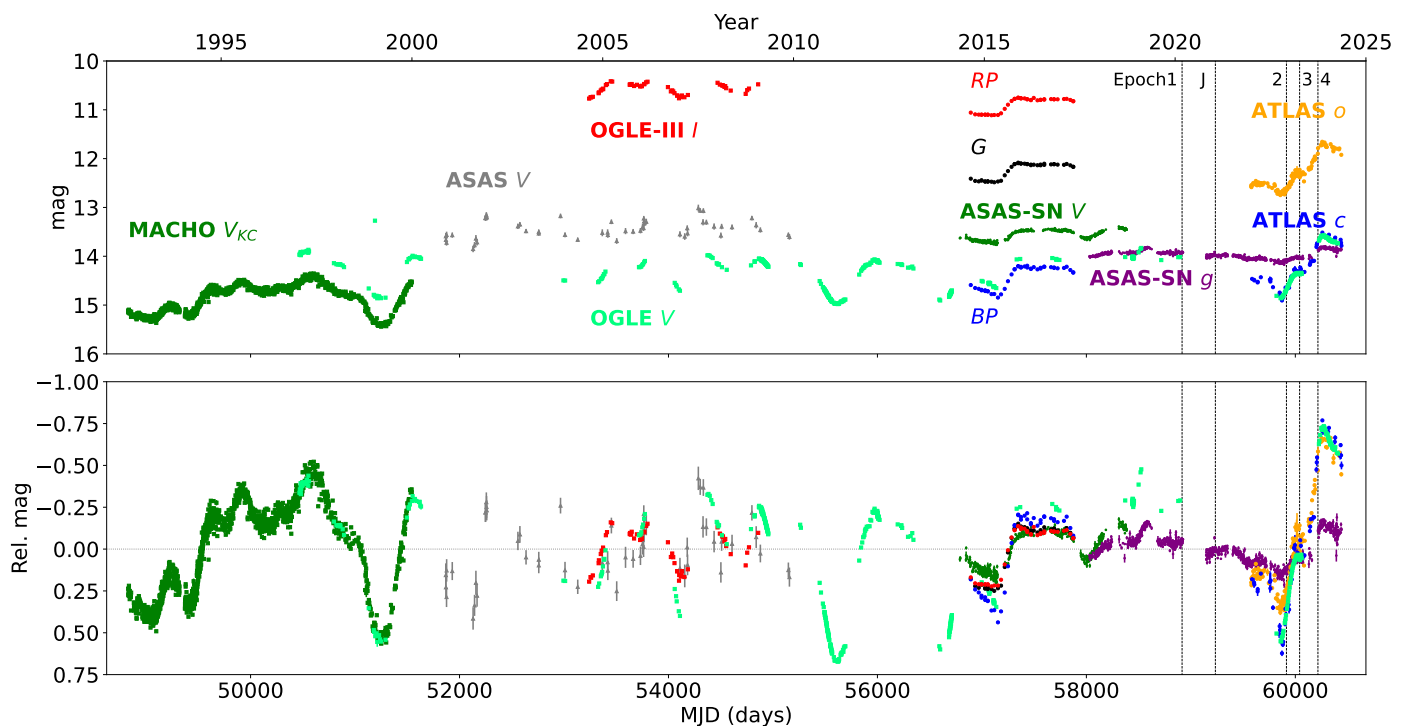


Fig. 3: *Top*: Light curve of [W60] B90 indicating the respective survey and filter. *Bottom*: Scaled light curves after subtracting the mean value. The vertical lines represent the epoch-spectroscopy as labeled in Table 1.

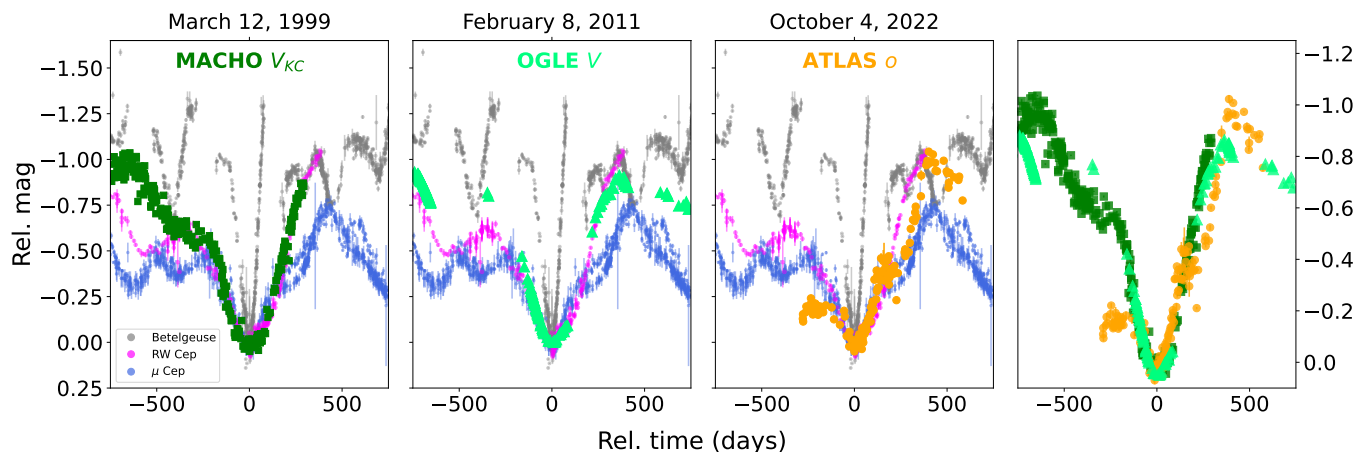


Fig. 4: The first three panels show the comparison of the three dimmings of [W60] B90 with the Great Dimming of Betelgeuse (grey), the dimming of RW Cep (magenta), and a minimum from μ Cep (blue) in the V -band from AAVSO. The right panel overplots the photometry of the three dimmings of [W60] B90. We used the minimum of each data set as the zero-point reference for each graph.

the largest dimming ($\Delta V \sim 0.8$ mag) of μ Cep in the last 50 yr, after the minimum in October 2015. We used the minimum of each event as the zero point for the relative magnitude and date. The first event in [W60] B90 occurred during the last years of the MACHO survey, between 1999 and 2000, reaching a minimum $V_{KC} = 15.4$ mag and abruptly rising $\Delta V_{KC} = 0.9$ mag after. The next major event is identified in the OGLE V -band data between 2011 and 2012, when it suffered another dimming increasing $\Delta V = 0.9$ mag, which was remarkably similar in time and brightness to the event in the MACHO data. The last major event occurred between October 2022 and November 2023, with the brightness increasing by $\Delta c \sim 1.3$ mag, $\Delta o \sim 1$ mag, and $\Delta V \sim 1.3$ mag. However, this event has a small discontinuity in

the rise, delaying the recovery compared to the other two events. The three events are 4350 and 4250 d apart, corresponding to an average recurrence period of approximately 11.8 years.

Apart from the three dimming events, we also noticed a variation in the photometric colors of [W60] B90 during three different minima in the light curve (Fig. 3). In general, a change to a redder color indicates a cooler atmospheric temperature, an increase in extinction due to dust formation, or both. The largest variation was observed by *Gaia* during the minimum in early 2015. $BP - RP$ increased to 3.75 mag, as it faded, but stabilized around 3.45 mag after the recovery. Furthermore, the OGLE data revealed another change in color around 54100 MJD, when a large offset was observed between filters V and I . However, the

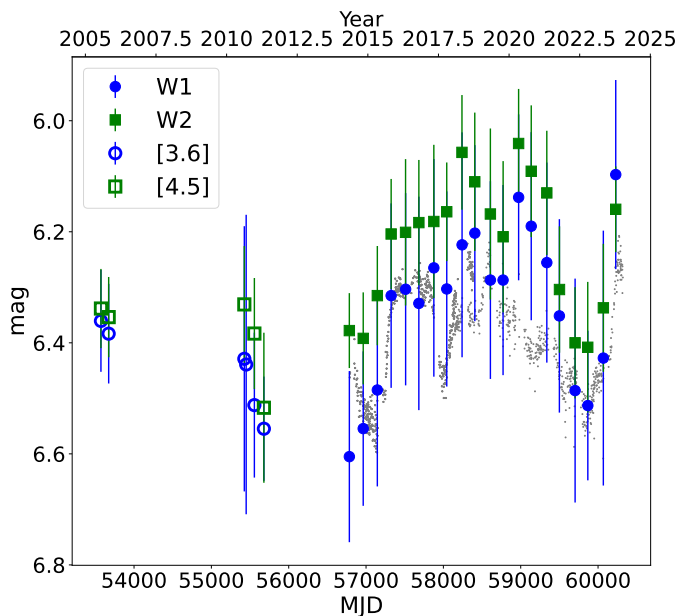


Fig. 5: Mid-IR light curve of [W60] B90 from NEOWISE and *Spitzer*. W1 and [3.6] are shown with full and open blue circles, respectively; W2 and [4.5] are shown with full and open green squares. ASAS-SN data are shown in grey with an offset for comparison.

poor sampling of the light curve prevents us from further analyzing this event. Lastly, the ATLAS $c - o$ color increased during the 2022 minimum. Follow-up spectroscopic observations after the minimum revealed a decrease in the T_{eff} and an enhancement of the extinction in agreement with the changing color (see Sect. 4.4). Remarkably, the color changes do not appear at every minimum, which suggests that specific conditions existed during these events.

4.2. Mid-IR light curve

Extreme RSGs do not only show variability in the optical range but may also vary significantly at longer wavelengths. Yang et al. (2018) have found a correlation between the mid-IR variability, luminosity, and mass-loss rate, with the latter confirmed by Antoniadis et al. (2024). Therefore, we analyzed the NEOWISE data and compared it with the variability of [W60] B90 in the optical (Fig. 5). The long-term variability of the data agrees with the optical trend from the ASAS-SN photometry. Contrary to the optical data, no short-term variations were observed. For example, the ASAS-SN data shows a decrease in the brightness at 58000 MJD, which is not detected in the NEOWISE bands. Higher cadence mid-IR photometry, as well as a comparison of optical to mid-IR photometry for other RSGs, is needed to confirm whether the short-term variations between the mid-IR and the optical are indeed decoupled.

The amplitude of the NEOWISE light curve is $\Delta W1 = 0.51$ mag and $\Delta W2 = 0.37$ mag. The data cover the last dimming event, yielding an amplitude $\Delta W1 = 0.42$ mag and $\Delta W2 = 0.25$ mag. We also calculated the median absolute deviation (MAD), a robust indicator to assess the variability, and found $\text{MAD}_{W1} = 0.0903$ and $\text{MAD}_{W2} = 0.0918$. Such a large MAD_{W2} places [W60] B90 in the top four RSGs with the highest MAD_{W2} in the LMC (see Fig. 17 in Yang et al. 2018). Hence, the large mid-IR variability agrees with the extreme nature of

[W60] B90: one of the most luminous RSG in the LMC with the third highest mass-loss rate for a single RSG (Antoniadis et al. 2024).

4.3. Periodicity

Periods $P_1 = 1006$ d and $P_2 = 453.44 \pm 0.04$ d have been derived using the MACHO data of [W60] B90 (Groenewegen et al. 2009; Groenewegen & Sloan 2018). Note that other studies reported $P = 776$ d (with $\Delta I_c = 0.39$ mag) from AAVSO photometry, and a long secondary period (LSP) of 4900 d, $\Delta m = 0.12$ mag from 50 yr of the digitized Harvard Astronomical Plate Collection (Watson et al. 2006; Chatys et al. 2019).

We used the period-luminosity (P-L) relations in the near and mid-IR (Yang & Jiang 2011) to calculate the predicted period and compare it with P_1 . We compiled the photometry of [W60] B90 in the bands J , H , K_s , [3.6], and [4.5] from the catalog of RSGs in the LMC published by Yang et al. (2018). We calculated the periods to be 829, 929, 1032, 1107, and 1041 d from $J = 8.37$, $H = 7.40$, $K_s = 6.83$, [3.6] = 6.29, and [4.5] = 6.29 mag, respectively. Despite the lack of error bars in $P_1 = 1006$ d, we consider the derived periods from H , K_s , [3.6], and [4.5] consistent with the expected. In fact, Yang & Jiang (2011) mentioned that K_s and [3.6] are the most reliable bands to use their P-L relations as they are the least affected by extinction and provide the tightest relations. As they did not deredden the photometry, RSGs with high A_V might differ from their predicted periods in the bands affected by extinction. Therefore, we attribute the shorter period from the J -band to the high extinction $A_V > 3$ mag reported for [W60] B90 (see Sect. 4.4).

4.4. Optical spectroscopy

We compared the optical spectra of the four epochs presented in Fig. 6 to analyze the evolution of the star with time. We detect changes in the shape of the SED and the depth of the TiO bands throughout the epochs, implying a spectral-type variation from M3 I to M4 I. Changes in the SED imply either a variation in the T_{eff} , $E(B - V)$, or both. Since the metallicity Z of the star does not change, the strength of the TiO bands is exclusively related to the T_{eff} (e.g. Levesque et al. 2007) and the wind of the star (Davies & Plez 2021), being deeper when the T_{eff} is cooler and the wind is stronger. We used the grid of MARCS models described in de Wit et al. (2023) to obtain the physical parameters for each spectral epoch. We primarily fit for T_{eff} and $E(B - V)$, keeping Z and $\log(g)$ fixed from the results in the J -band (see Sect. 4.6). We derived $Z = -0.25$ dex and $\log(g) = +0.5$ dex from the local thermodynamic equilibrium (LTE) MARCS models, in contrast to de Wit et al. (2023) which assumed a LMC-like metallicity ($Z = -0.38$ dex) and obtained $\log(g) = -0.2$ dex from the Ca II triplet. The discrepancy in $\log(g)$ does not affect our fit in the optical as the TiO bands are temperature indicators and not sensitive to gravity. Finally, we performed the fitting in two stages. In the first iteration, we fitted spectral regions including shorter wavelengths to constrain the shape of the SED and get more accurate values for $E(B - V)$. Then, fixing $E(B - V)$ in the second iteration, we only use spectral regions affected by the TiO bands to obtain the T_{eff} of the star. The best-fit models to each epoch are shown in Fig. 7 and their parameters are shown in Table 3.

We obtained Epoch1 at the beginning of 2020 when the RSG exhibited low-amplitude variability (see Fig. 3). Indeed, the fit of Epoch1 reveals the lowest χ^2 among our sample, implying minor deviations from the model spectra, suggesting the

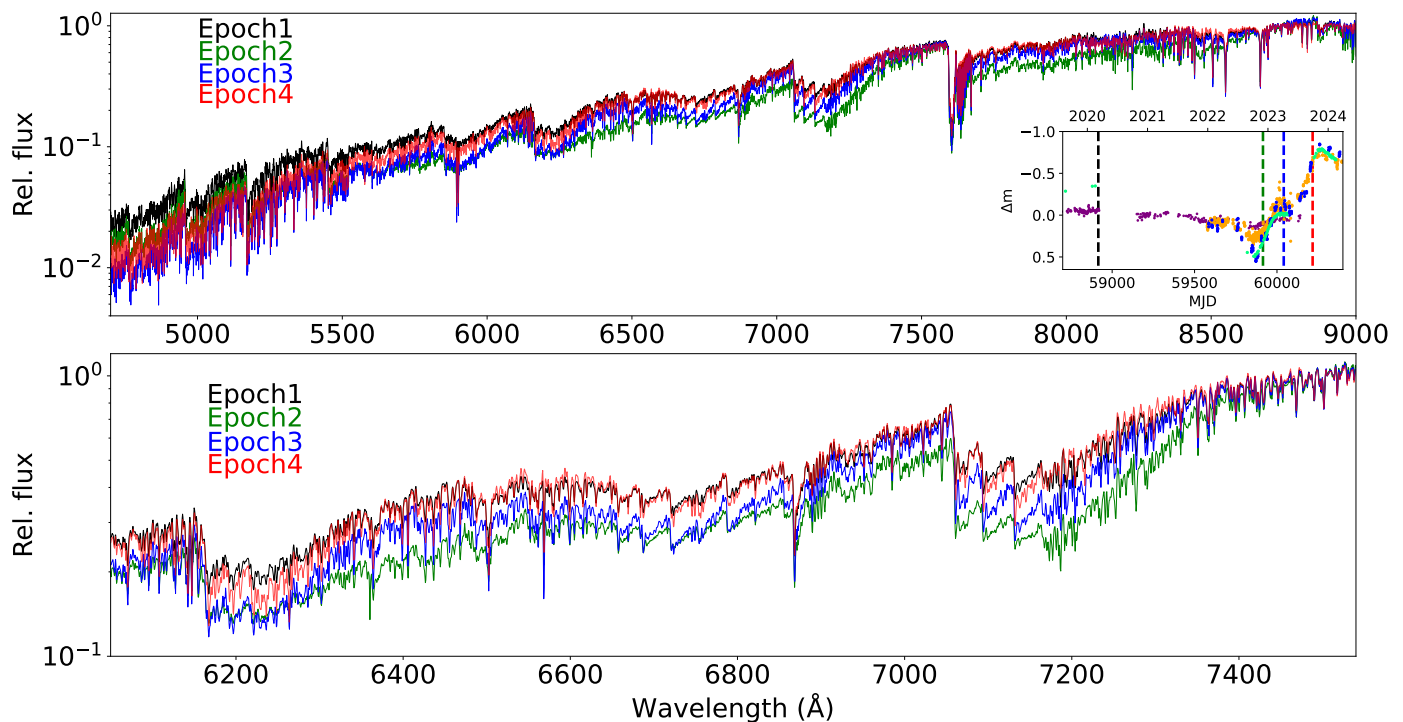


Fig. 6: Comparison of the spectroscopic epochs of W60 [B90] in the optical (*top*) and the main TiO bands at 6150 and 7050 Å (*bottom*). The inset shows the light curve (as in Fig. 3) indicating each spectroscopic epoch with the dashed lines, following the color code of the spectra.

RSG atmosphere was stable. During the following years (2020–2022), the brightness decreased $\Delta g = 0.3$ mag in ASAS-SN, although the real change in brightness might be larger (see discussion in Sect. 4.1). We obtained Epoch2 two months after the photometric minimum. This spectrum reveals the strongest TiO bands of all epochs, implying either a decrease in the T_{eff} , an increase of \dot{M} , or a combination of both. The spectrum suggests a complex atmospheric structure following the photometric minimum, which cannot be reproduced by a single MARCS model (see Sect. 4.5), and we consider the T_{eff} and the $E(B - V)$ derived for Epoch2 to be unreliable. We obtained Epoch3 four months later, when the RSG exhibited a plateau during the recovery, after initially increasing $\Delta o = 0.5$ mag compared to the minimum. It shows weaker TiO bands than Epoch2, and we found a higher best-fit T_{eff} according to this change. However, $E(B - V)$ is considerably higher than the previous epochs, implying that the extinction in the line of sight increased after the minimum. Finally, we obtained Epoch4 two months before the maximum in late 2023. In this epoch, it was brighter than Epoch2 by $\Delta o = 0.9$ mag, and the RSG exhibited the highest measured T_{eff} . The SED is not as extinct as in Epoch3 but is steeper than in the first two spectra, in agreement with the derived $E(B - V)$.

4.5. Spectroscopy during the dimming (Epoch2)

The Great Dimming of Betelgeuse was explained by a clump of dust in the line of sight or, alternatively, a cold patch in the atmosphere (Montargès et al. 2021). We attempted to model the latter by creating a grid of composite MARCS models. We created composite models from the superposition of two single models ($T_{\text{eff}1}$ and $T_{\text{eff}2}$) with weighted fluxes from each model in steps of 20% (e.g., 80–20% or 60–40%). We used T_{eff} from 3300–4500 K in

steps of 50 K and assumed $Z = -0.25$ dex and $\log(g) = -0.2$ dex as in Sect. 4.4.

We obtained the best fit for 60% of $T_{\text{eff}1} = 3300$ K, 40% of $T_{\text{eff}2} = 4500$ K, $E(B - V) = 1.2$ mag, and $\chi^2 = 62.4$. The composite model considerably improves the fit, but the temperatures found are at the edges of the grid. Fixing $T_{\text{eff}1} = 3950$ K using the result of EpochJ (see Sect. 4.6), we derived the best fit for 60% of $T_{\text{eff}1} = 3950$ K to be 40% of $T_{\text{eff}2} = 3300$ K and $E(B - V) = 1.25$ mag, with a $\chi^2 = 68.2$ (Fig. 8), again finding a $T_{\text{eff}2}$ at the edge of the grid. Nevertheless, we argue that the MARCS models cannot always reproduce the real photosphere of an extreme RSG. Physical processes such as 3D assumptions, wind, or magnetic fields, are currently missing in the MARCS models recipes. Hence, a new generation of models including these processes is needed to properly reproduce the complete nature of RSGs.

4.6. Near-IR spectroscopy

We applied the non-LTE (NLTE) MARCS models (Bergemann et al. 2012, 2013, 2015) to fit the atomic lines in the *J*-band of our FIRE spectrum. We created a grid of models with a range $T_{\text{eff}} = 3300$ –4500 K in steps of 25 K, $\log(g) = -0.5, +0.5$ dex in steps of 0.25 dex, microturbulent velocities from 2.5 to 5.5 km s⁻¹ in steps of 0.5 km s⁻¹ and $Z = -0.38, -0.25, -0.1, +0.0$ and $+0.2$ dex. Also, we used the LTE grid presented in the previous section to compare the results from the NLTE models with the canonical MARCS models. We found the best-fit model with reduced χ^2 and the uncertainties from the 1σ interval of the distribution. We followed the approach presented in Patrick et al. (2017) and fitted the lines Fe I $\lambda\lambda 1.178327, 1.188285, 1.197305$, Si I $\lambda\lambda 1.198419, 1.199157, 1.203151$, Mg I $\lambda\lambda 1.208335$ and Ti I $\lambda\lambda 1.189289, 1.194954$. We

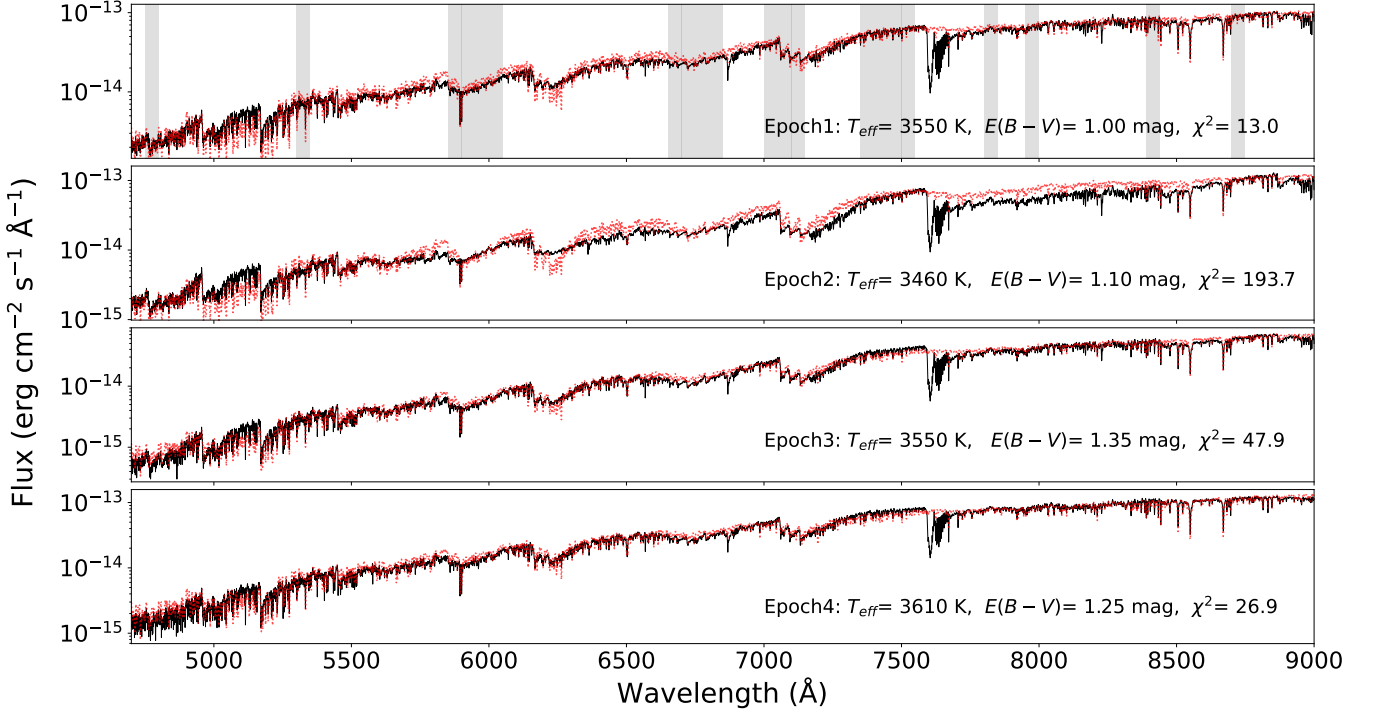


Fig. 7: Best MARCS model fit (red) for each epoch from MagE (black). Shaded areas in Epoch 1 show the spectral regions used in the fitting.

Table 3: Physical parameters of [W60] B90 from spectroscopy

Atomic lines in the J -band ^a						
Name	Model	Z (dex)	$T_{\text{eff},J}$ (K)	$\log(g)$ (dex)	χ^2	
EpochJ	MARCS LTE	$-0.25^{+0.25}_{-0.12}$	3970^{+130}_{-280}	$-0.20^{+0.20}_{-0.30}$	63.1	
	MARCS NLTE	$+0.00^{+0.20}_{-0.10}$	3900^{+150}_{-100}	$+0.50^{+0.00}_{-0.75}$	36.4	
TiO bands from the optical						
	Spectral type	ATLAS o (mag)	$T_{\text{eff},\text{TiO}}$ (K)	$E(B-V)$ (mag)	A_V^b (mag)	χ^2
Epoch1 ^c	M3 I	–	3550 ± 40	1.00 ± 0.15	3.41 ± 0.51	13.0
Epoch2	M4 I	12.6 ± 0.1	3460^{+20}_{-30}	1.10 ± 0.10	3.75 ± 0.34	193.7
Epoch3	M3 I	12.3 ± 0.1	3550^{+40}_{-30}	$1.35^{+0.10}_{-0.05}$	$4.60^{+0.34}_{-0.17}$	47.9
Epoch4	M3 I	11.8 ± 0.1	3610^{+60}_{-50}	$1.25^{+0.10}_{-0.05}$	$4.26^{+0.34}_{-0.17}$	26.9

Notes. ^(a) Assuming $Z = -0.25$ dex and $\log g = -0.2$ dex from the J -band fit. ^(b) Converted from $E(B-V)$ assuming $R_V = 3.41$. ^(c) $T_{\text{eff}} = 3570^{+60}_{-50}$ K and $E(B-V) = 1.00 \pm 0.14$ mag from de Wit et al. (2023).

excluded the line Mg I $\lambda\lambda 1.182819$ because the feature on the right wing of the line profile is not in the models and could compromise the diagnostic of the line. Similarly, we rejected Si I $\lambda\lambda 1.210353$ due to the difficulty of establishing the continuum level during the fit. Nevertheless, both lines are satisfactorily reproduced by the best-fit model probing that their rejection did not compromise the result.

The results presented in Fig. 9 and Table 3 show a strong disagreement of $\gtrsim 300$ K between the T_{eff} derived from the TiO bands ($T_{\text{eff},\text{TiO}}$) in the optical spectra and the atomic lines fit in

the J -band ($T_{\text{eff},J}$). The NLTE models constrain the $T_{\text{eff},J}$ better than the LTE models, although both results are consistent within the errors. Both indicate higher Z than the commonly $Z = -0.38$ dex assumed for the LMC, with the LTE models suggesting a slightly higher Z than the LMC, while the NLTE models favor a solar Z . The $\log(g)$ results are poorly constrained as the errors span over the whole range of the grid. The best NLTE model finds $\log(g) = +0.50^{+0.00}_{-0.75}$ dex, similar to what de Wit et al. (2023) derived from the Ca II triplet in Epoch1 and consistent within error with the LTE result $\log(g) = -0.2^{+0.20}_{-0.30}$ dex as

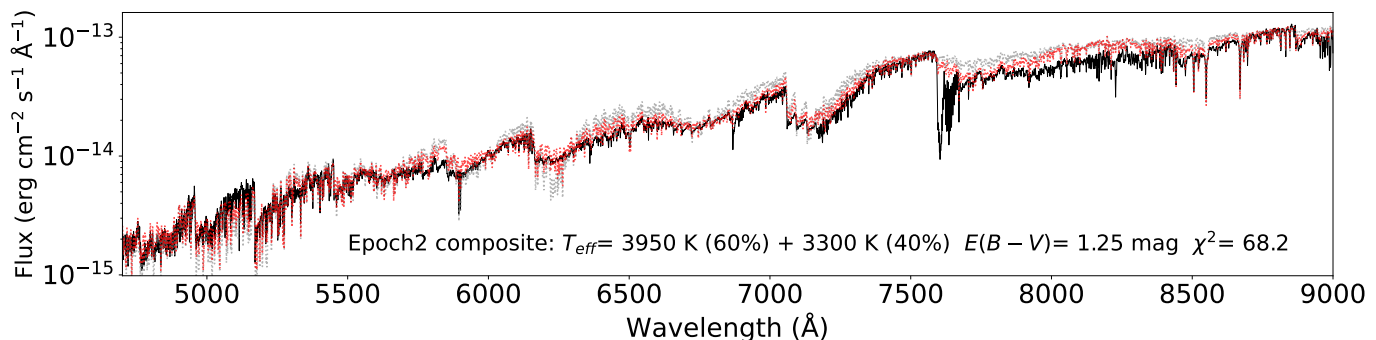


Fig. 8: Comparative of the best composite model (red) with the 60% of the flux from a single $T_{\text{eff}1} = 3950$ K and the 40% from $T_{\text{eff}2} = 3300$ K, and the best single model (grey) from Fig. 7 for Epoch 2.

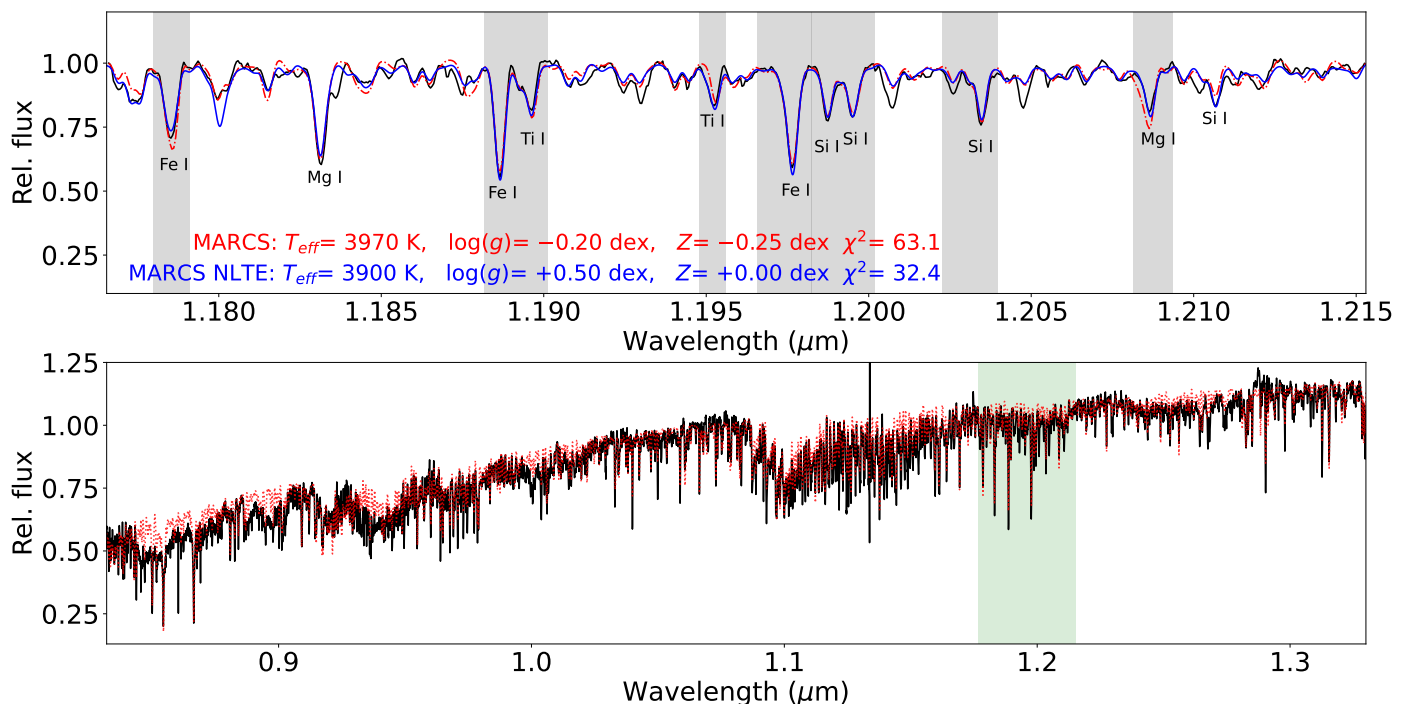


Fig. 9: *Top*: Best fits of FIRE spectrum (solid black) in the J -band for the canonical MARCS models (dashed-dot red) and the NLTE corrected version (solid blue). The spectral regions used in the fitting are shown with grey shades. The indicated lines have been corrected for NLTE effects. *Bottom*: Best MARCS model (dotted red) from the J -band to the FIRE spectrum (black). The model was reddened with $E(B - V) = 1.05$ mag to match the SED. The green-shaded region highlights the spectral region shown in the upper plot.

the best solution. We applied $\log(g)$ and Z from the LTE result to constrain the physical parameters in the optical for consistency, as the TiO bands do not have NLTE correction (see Sect. 4.4). Therefore, using $Z = +0.00$ from the NLTE in the optical instead of $Z = -0.25$ would lead to an overestimation of the abundances, affecting the $T_{\text{eff,TiO}}$. However, the discrepancy in $\log(g)$ between the LTE and the NLTE result is negligible as the TiO bands are not sensitive to this parameter.

5. Discussion

5.1. Bow shock, bar and runaway status

Only three single Galactic RSGs with a bow shock have been previously identified: Betelgeuse, IRC-10414, and μ Cep. Par-

ticularly, Betelgeuse exhibits a bar at 0.5 pc from the star (assuming a distance of 200 pc; Harper et al. 2008, 2017), which remains unexplained. It might be the relic of the blue supergiant (BSG) wind interaction with the ISM, just before Betelgeuse recently became a RSG (Mackey et al. 2012). Contrarily, Decin et al. (2012); Meyer et al. (2021) proposed an interstellar origin for the bar that could be the edge of an interstellar cloud illuminated by Betelgeuse or a linear filament in the interstellar cirrus. In the case of [W60] B90, there is a bar structure at 1 pc, which is partially shocked, only in the southeastern part. The movement of [W60] B90 towards the bar and the shocked material found between them and in the bar confirms a causal connection. However, the interpretation of our findings requires further work and is beyond the scope of this paper. The scenario of a BSG wind

interaction is plausible, but can only hold if [W60] B90 recently became a RSG or it underwent a blue loop during the RSG phase (see Sect. 5.7 and Meynet et al. 2011).

[W60] B90 moves towards the bar with a peculiar velocity between $16 - 25(\pm 11)$ km s⁻¹ (Table A.1). Given that hydrogen is the most abundant element in the gas, we can assume that it is a good tracer of the CSM and use the ~ 10 km s⁻¹ difference in RV between H α and the star to construct the 3D velocity. Therefore, [W60] B90 moves with a $19 - 27(\pm 11)$ km s⁻¹ velocity, establishing it as a walkaway star, on the brink of the runaway limit (>30 km s⁻¹; Renzo et al. 2019). Further releases from *Gaia* will improve the uncertainties on the peculiar velocity, allowing us to trace back its movement, discern its birthplace, and speculate the cause of its ejection, either by dynamical interactions or from a SN kick (Stoop et al. 2023). Nevertheless, the walkaway status does not conflict with the bow shock scenario. The speed of sound in the low-density isothermal warm neutral medium is on the order of ~ 1 km s⁻¹ (Cox et al. 2012). Therefore, the RSG would move supersonically in the medium even considering the lower limit (>5 km s⁻¹). The peculiar velocity, the RV of the ions, and the ratios in Appendix C are consistent with the low-velocity shock scenario (<100 km s⁻¹).

Apart from detecting shocked material where the bow shock is expected, we also find enhanced [S II]/H α at northern positions close to the star. This might indicate a non-homogeneous CSM and clumpy, asymmetric mass-loss events. Observations in the mid-IR have shown multiple arcs and similarly strong asymmetries in the CSM of Betelgeuse. Decin et al. (2012) demonstrated that a combination of anisotropic mass-loss processes and the influence of galactic magnetic fields might explain the multiple arcs and clumps around Betelgeuse. Further observations are needed to spatially resolve the circumstellar environment of [W60] B90. Identifying the hypothesized bow shock or non-homogeneous structures around the star would help to constrain the recent mass-losing history of [W60] B90.

5.2. Properties of the dimming events

Our spectroscopic analysis revealed physical properties similar to those of Betelgeuse during the Great Dimming (see Sect. 4.5 and 5.3), therefore, we speculate that the same physical mechanism drives both events. MacLeod et al. (2023) explained the Great Dimming as a result of a hot convective plume that forms in the turbulent envelope, breaking free from the surface and triggering a mass ejection. However, the Great Dimming displayed a more abrupt brightness rise on a shorter timescale (~ 200 d) than the rise of the events of our RSG (~ 400 d). The radius of [W60] B90 is $\sim 1200 R_{\odot}$, while that of Betelgeuse is reported to be between $750-1000 R_{\odot}$ (Joyce et al. 2020; Kravchenko et al. 2021). Contrarily, μ Cep ($1259 R_{\odot}$; Josselin & Plez 2007) and the Galactic hypergiant RW Cep ($900-1760 R_{\odot}$; Anugu et al. 2023) have a comparable radius to [W60] B90, and both stars exhibit a similar rise after the minima (Fig. 4). We speculate that the timescale of these events is related to the radius of the stars, as a more extended atmosphere needs more time to stabilize. The same idea was presented in the analysis of the dimming of RW Cep (Anugu et al. 2023), which revealed a surface mass ejection that created a dust cloud and partially blocked the stellar photosphere. Although this is the only dimming event observed for RW Cep, the dust shells detected around the hypergiant suggest that it may have undergone several mass ejections over the last century (Jones et al. 2023). The dimming events of [W60] B90 have a recurrence of ~ 11.8 yr, while the dimming of μ Cep is unique over the past 50 yr and the Great Dimming of Betelgeuse

is a unique event over the last 100 yr. Moreover, the rising plume on Betelgeuse disturbed its pulsation period, switching from the ~ 400 d fundamental period to the ~ 200 d overtone (MacLeod et al. 2023). We do not find a change in the periodicity in any of the three dimmings. Extending the study of long-term variability to other luminous RSGs is needed to understand how common such events are, and whether they are indeed related to the stellar radius. Spatially resolving the CSM of [W60] B90 will reveal if there are structures correlated with the 11.8 yr period of the dimmings.

The fundamental period $P_1 = 1006$ d (Groenewegen & Sloan 2018) and the 4900 d LSP of [W60] B90 are considerably larger than the fundamental $P \sim 400$ d (Kiss et al. 2006) and the 2000-2365 d LSP (Chatys et al. 2019; Joyce et al. 2020) of Betelgeuse. They are also consistent with the expected P from the P-L relations and the higher luminosity of [W60] B90. Although Chatys et al. (2019) do not provide errors, their 13.5 yr LSP of [W60] B90 is suspiciously close to the 11.8 yr of the dimming recurrence found in this paper. Furthermore, the periods found in [W60] B90 are remarkably similar to the fundamental period $P=880$ d and LSP of 4400 d of μ Cep. Although this RSG is reported to be comparable in luminosity and radius to [W60] B90 (see Sect. 5.6), no recurrence of dimming events has been reported in μ Cep to date.

5.3. Spectral variability

The TiO bands are the primary spectroscopic feature for classifying M-stars in the optical. Dorda et al. (2016) found that 30% of the ~ 500 RSGs in their LMC sample showed spectral type variability with a mean change of two spectral subtypes. They also reported that cool RSGs are more likely to exhibit spectral-type changes. In the case of [W60] B90, we found the depth of the TiO bands to vary among the epochs, yielding a spectral type of M3 I in Epoch1 (de Wit et al. 2023) and M4 I in Epoch2. However, observations of the star during its maximum and minimum would likely yield larger spectral variability. These results demonstrate the uncertainty of spectroscopically classifying variable RSGs based on a single observation.

A tomographic analysis of μ Cep and Betelgeuse explained the correlation between $T_{\text{eff,TiO}}$ and the optical variability as an effect of the convective cells in the atmosphere (Kravchenko et al. 2019, 2021). The $T_{\text{eff,TiO}}$ and the brightness decrease as the material rises, while both increase once it falls, creating a hysteresis loop between the RV of the atomic lines and the $T_{\text{eff,TiO}}$. We report a similar trend between $T_{\text{eff,TiO}}$ and the optical variability for [W60] B90 during the brightening in 2022. The Epoch2 spectrum was obtained 2 months after the minimum in 2022, showing spectral features incompatible with single MARCS models. Montargès et al. (2021) explained the Great Dimming as a large cold spot rising in the atmosphere of Betelgeuse. Big convective cells at different temperatures can create large cold spots that cause deeper TiO bands, decreasing the brightness in the optical. Furthermore, if convection is strong enough, it can result in a mass ejection (MacLeod et al. 2023; Drevon et al. 2024). This scenario is consistent with the enhanced extinction reported in the epochs following the minimum Epoch3 and Epoch4, where A_V changes from 3.41 ± 0.51 mag before the event to $4.60^{+0.34}_{-0.17}$ mag several months after. This demonstrates the importance of using the light curve to interpret whether the RSG was observed during a stable state, or during a brief minimum or maximum. Further investigation is needed to reveal the origin of the hysteresis loops and how they are related to episodic mass-loss events.

5.4. $T_{\text{eff,TiO}}$ vs. $T_{\text{eff,J}}$

We found a strong discrepancy in T_{eff} when we obtained the physical parameters from different spectral ranges. While the TiO bands in the optical suggest $T_{\text{eff,TiO}} \approx 3550$ K, we derived $T_{\text{eff,J}} = 3900$ K from the atomic lines in the J -band. Davies et al. (2013, 2015) already reported a discrepancy in T_{eff} derived from the TiO bands compared with the J -band or the SED fits, which is related to the formation zone of each diagnostic. However, if the MARCS models were consistent, one single model would describe the atmosphere of the star with one single T_{eff} . Given these discrepancies, de Wit et al. (2024) derived a T_{eff} scaling relation based on the MARCS models to scale $T_{\text{eff,TiO}}$ to a more secure T_{eff} . Using their relation, we find $T_{\text{eff,J}} = 3960$ K, which is consistent with our results.

Previous studies on luminous RSGs have also reported very cool $T_{\text{eff,TiO}}$, which cannot be reproduced by the theoretical evolutionary models (e.g. Levesque et al. 2007; de Wit et al. 2024). Davies & Plez (2021) demonstrated that adding a \dot{M} to the MARCS models results in an enhancement in the TiO band strengths, similar to the effect of decreasing the T_{eff} . The $T_{\text{eff,TiO}}$, therefore, might be underestimated in evolved luminous RSGs with strong \dot{M} as the MARCS models do not account for it. Recently, by implementing \dot{M} to the MARCS models, González-Torà et al. (2023) were able to reconcile spectral features in the near and mid-IR that did not match with the canonical MARCS models. Our results reinforce the urgent need for a complete grid of models with \dot{M} to break the degeneracy in the optical and reconcile the $T_{\text{eff,TiO}}$, the $T_{\text{eff,J}}$ and the evolutionary models. Extending the 1D LTE assumptions from the MARCS models to 3D magneto-hydrodynamic ones will also improve the modeling of the strong convection in RSGs (e.g. Kravchenko et al. 2019; Ma et al. 2024)

Furthermore, the addition of NLTE corrections to the MARCS models for the atomic lines in the J -band considerably impacts the results. It decreases the uncertainty in T_{eff} and it reveals a high metallicity ($Z = +0.00^{+0.20}_{-0.10}$ dex), which is inconsistent with the mean metallicity of the LMC ($Z = -0.37 \pm 0.14$ dex; Davies et al. 2015). Although it is more metal-rich than expected for the LMC, [W60] B90 is not the first cool supergiant with solar-like Z , as six more cases are already known in the LMC (Tabernero et al. 2018). The solar Z , however, conflicts with the low- Z environment suggested by the faint nitrogen nebular emission. The enhanced Z can be explained by extra rotational mixing occurring in its interior during its evolution enhancing the metal content in the surface, by a binary history with mass-transfer changing the abundances, or even a merger with a companion.

5.5. Binarity

Recent works have estimated the fraction of RSGs in binary systems to be at least 15% (Dorda & Patrick 2021; Patrick et al. 2022). We explored the RV variations from the Ca II triplet (Table 4) and found all epochs to be consistent with the *Gaia* DR3 value, except for Epoch3. We can not attribute the difference of less than 10 km s^{-1} to the presence of a companion, as tomographic studies have revealed that such variations can be explained by the rising and falling of material in the atmosphere (Kravchenko et al. 2019, 2021). A pilot study by Patrick (2020) suggested a correlation between the RV variations and the luminosity of the RSGs, which might be connected to stronger hysteresis loops. Since [W60] B90 is close to the observed upper luminosity of RSGs in the LMC (Davies et al. 2018), it is expected to have larger variability and RV differences. Therefore, we argue that the small discrepancy in the RV is a combined

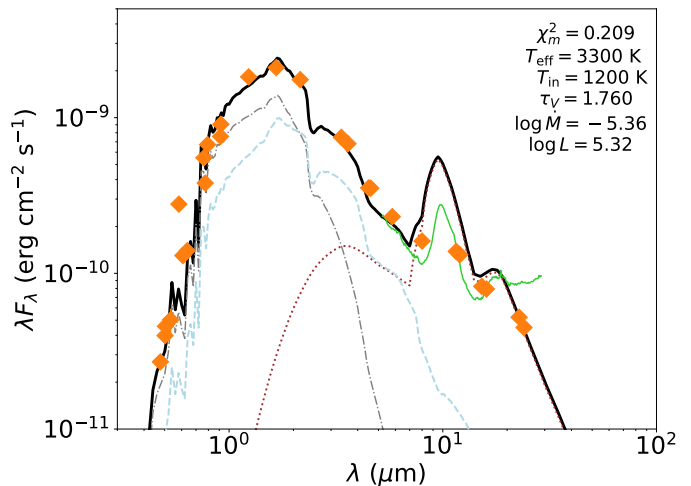


Fig. 10: SED of [W60] B90. The orange diamonds show the observations and the black line is the best-fit model from DUSTY, which is a superposition of attenuated flux (dashed light blue), the scattered flux (dot-dashed grey), and dust emission (dotted brown). The green curve represents the *Spitzer* IRS spectrum.

effect of the changes in the atmosphere due to its evolutionary status and the intrinsic error of $\pm 7 \text{ km s}^{-1}$ from the observations. Moreover, *Gaia* DR3 indicators such as the RUWE, astrometric excess noise, and binary probability parameter do not support a binary scenario. We also report the absence of a counterpart in *Swift* observations and the non-detection of blue excess in the SED, disfavouring a hot companion. Therefore, we conclude that [W60] B90 is currently a single star given the total lack of evidence for a companion.

Table 4: Radial velocity of Ca II triplet

Spectrum	RV (km s^{-1})
Epoch1	264 ± 4
EpochJ	268 ± 2
Epoch2	261 ± 3
Epoch3	272 ± 2
Epoch4	266 ± 3
<i>Gaia</i> DR3	263.49 ± 1.02

Notes. Spectral resolution error is $\pm 7 \text{ km s}^{-1}$.

5.6. Mass-loss rates

Antoniadis et al. (2024) determined the mass-loss rates of over 2000 RSGs in the LMC using the radiative transfer code DUSTY, finding $\dot{M} = 5.1^{+5.1}_{-1.7} \times 10^{-6} \text{ M}_{\odot} \text{ yr}^{-1}$ for [W60] B90. In this work, we recomputed the \dot{M} with identical assumptions, but including synthetic photometry from the IRS spectrum (see Sect. 2.4) to improve the SED fitting. We present the new fit in Fig. 10, which results in $\dot{M} = 4.4^{+5.1}_{-1.7} \times 10^{-6} \text{ M}_{\odot} \text{ yr}^{-1}$ with a best-fit optical depth $\tau_v = 1.76$ for the best fit of $T_{\text{eff}} = 3300$ K and inner dust shell temperature $T_{\text{in}} = 1200$ K (for the description of the fitted parameters see Antoniadis et al. 2024). This \dot{M} makes [W60] B90 the third highest mass-losing probably single RSG in the Anto-

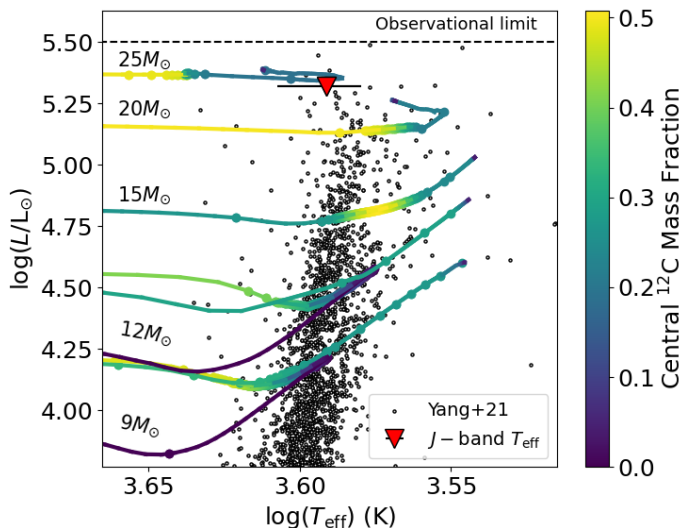


Fig. 11: Location of [W60] B90 (red triangle) in the Hertzsprung-Russell diagram of the RSG population in the LMC (black dots, Yang et al. 2021). The observed upper luminosity limit for RSGs is represented with the dashed line. The color map represents the central ^{12}C mass fraction on the MIST evolutionary track, while the nodes indicate a step of 10^4 yr.

niadis et al. (2024) sample. Moreover, it is the second highest M_{dust} among the oxygen-rich stars in the study of evolved stars in the LMC from Riebel et al. (2012). These results underline the extreme nature of [W60] B90 and agree with it being one of the most variable RSGs in the mid-IR in the LMC (Yang et al. 2018).

From the properties of a bow shock, one can derive the mass-loss rate of the producer. Therefore, we compare the mass-loss rate and the general properties of [W60] B90 with the three known, Galactic RSGs with a bow shock in Table 5. All of them have considerable mass-loss ($\dot{M} > 10^{-6} M_{\odot} \text{ yr}^{-1}$) and high luminosity ($\log(L/L_{\odot}) > 5.0$ dex). IRC-10414 and μ Cep are fast runaways, while Betelgeuse is at the limit between a walkaway and a runaway star. Remarkably, Betelgeuse is the most compact of the RSGs, exhibiting shorter periods, while [W60] B90 and μ Cep have comparable periodicity (see Sect. 5.2). However, none of the physical properties stand out as a common signature of a bow shock. External factors to the RSGs such as their environment or the specific evolution likely determine the formation of a bow shock.

5.7. Evolutionary status

We explore the location of [W60] B90 in the Hertzsprung-Russell diagram using the derived $T_{\text{eff},J} = 3900_{-100}^{+150}$ K (see Table 3) and $\log(L/L_{\odot}) = 5.32 \pm 0.01$ dex (Antoniadis et al. 2024). Similar to de Wit et al. (2023), we compare its location to the LMC catalog of RSGs from Yang et al. (2021). We also used the MIST models (Dotter 2016; Choi et al. 2016) of rotating single stars ($v = 0.4v_{\text{crit}}$) in the range of 8 to 25 M_{\odot} . The position of [W60] B90 consistently matches the $M_{\text{ini}} = 25 M_{\odot}$ track, being more massive than Betelgeuse ($M_{\text{ini}} = 18 - 21$; Joyce et al. 2020), with current carbon burning in the core and within the last two nodes of the evolutionary track. Therefore, following the expected evolution for a RSG, [W60] B90 should explode as a Type II SN within the next 10^4 yr (Smartt et al. 2009). However, the observational lack of massive RSGs exploding as SNe

(the so-called ‘RSG problem’; Smartt 2009, 2015) suggests that either they end their lives in warmer states by stripping part of their envelopes or they collapse into black holes without exploding. Although determining the future evolution of [W60] B90 is beyond the scope of this paper, monitoring this evolved massive RSG could shed light on the ‘RSG problem’ and indicate whether episodic mass-loss influences the fate of RSGs.

6. Summary and conclusions

We present a detailed study of the very luminous RSG [W60] B90 ($\log(L/L_{\odot}) = 5.32$ dex), motivated by the discovery of a bar-like structure at 1 pc, which is reminiscent of the bar around Betelgeuse. We found [W60] B90 to be a walkaway star, with a supersonic peculiar velocity between 16–25 (± 11) km s^{-1} in the direction of the bar. We also obtained optical long-slit spectroscopy of the circumstellar environment of [W60] B90 to search for evidence of the hypothesized bow shock. We used the criterion $[\text{S II}]/\text{H}\alpha > 0.4$ to reveal the shocked origin of the nebular emission in the southern part of the bar, which confirms a causal connection with the RSG, and between the bar and the star, where the bow shock is expected. Therefore, [W60] B90 is the first extragalactic RSG with a suspected bow shock.

We compiled archival photometry to construct the optical light curve spanning more than 30 yr, reporting three dimming events in the optical with a recurrence of ~ 11.8 yr and $\Delta V \sim 1$ mag. We notice a similar recovery timescale of ~ 400 d for each dimming event in [W60] B90, in contrast with the Great Dimming of Betelgeuse that lasted ~ 200 d. We attributed the delay in the recovery to the size of the atmosphere, as [W60] B90 is more extended than Betelgeuse and the adjustment within the atmosphere needs additional time to manifest. We reinforce this argument by reporting similarities in the timescale between the dimmings of [W60] B90 with those of μ Cep and the hypergiant RW Cep (Anugu et al. 2023), which are comparable in size to our RSG. We also assemble a 10 yr mid-IR light curve reporting a long-term variability correlation with the optical and an amplitude $\Delta W1 = 0.51$ mag and $\Delta W2 = 0.37$ mag, and $\Delta W1 = 0.42$ mag and an amplitude $\Delta W2 = 0.25$ mag during the last dimming event.

Optical multi-epoch spectroscopy during the recovery of the last dimming event revealed different atmospheric properties for each epoch and spectral variability (from M3 I to M4 I), highlighting the importance of a light curve to assess the current state of variable RSGs. We noticed a correlation in the $T_{\text{eff,TiO}}$ and brightness of the star, which might be connected to convection (Kravchenko et al. 2019, 2021). We detect an enhancement of A_V after the dimming, which suggests an addition of dust in the line-of-sight, as a consequence of a mass ejection during the minimum. In addition, a single model can not reproduce the complex atmosphere of the star during the closest epoch to the minimum. A composite model of cool and hot components considerably improves the description of the spectral features observed. We conclude that [W60] B90 suffered a mass ejection, similar to that reported during the Great Dimming of Betelgeuse (Montargès et al. 2021; Dupree et al. 2022) and the dimming of RW Cep (Anugu et al. 2023). Furthermore, we found solar-like metallicity $Z = 0.0_{-0.1}^{+0.2}$ dex from the atomic lines in the J -band, which might indicate the evolved state of [W60] B90 and the prior mixing in the stellar interior entailing an overabundance of metals on the surface. We also report incompatible differences of $\Delta T_{\text{eff}} > 300$ K between the diagnostic in the J -band and the optical TiO bands. New models are urgently needed as the current ones are inconsistent depending on the spectral range observed.

Table 5: Parameters of [W60] B90 compared to the three known RSGs with a bow shock

Name	Sp. type	$T_{\text{eff,TiO}}$ (K)	$\log(L/L_{\odot})$ (dex)	Radius (R_{\odot})	\dot{M} ($10^{-6} M_{\odot} \text{ yr}^{-1}$)	P (d)	LSP (d)	v_{pec} (km s^{-1})	Reference
[W60] B90	M3 I	3550 ± 40	5.32 ± 0.01	1210	$4.4^{+5.1}_{-1.7}$	1006	4900	16-25	This work, (1)
Betelgeuse	M2 I	3650 ± 25	5.10 ± 0.22	750 – 1000	1 – 4	388	2050	30	(2-5)
IRC-10414	M7 I	3300	5.2	1200	<10	768	-	70	(6)
μ Cep	M2 Ia	3750 ± 20	5.45 ± 0.40	1259	1.7^a	860	4400	80	(7-9)

Notes. ^(a)Converted from \dot{M}_{dust} assuming a gas-to-dust ratio of 200.

(1) Antoniadis et al. (2024), (2) Levesque et al. (2005), (3) Joyce et al. (2020), (4) Kravchenko et al. (2021), (5) Le Bertre et al. (2012), (6) Gvaramadzé et al. (2014), (7) Josselin & Plez (2007), (8) Jones et al. (2012) (9) Tetzlaff et al. (2011)

Basic properties of RSGs such as NLTE assumptions, the wind of the star, convection, or magnetic fields need further study to construct the new generation of RSG models.

The detection of shocked material in the CSM, the high mass-loss rate ($\dot{M} = 4.4^{+5.1}_{-1.7} \times 10^{-6} M_{\odot} \text{ yr}^{-1}$), the high variability reported in the optical and the mid-IR, and the changes in the extinction after the minimum in 2022 suggest that [W60] B90 is in an unstable evolutionary state and undergoing episodes of mass loss. Its location in the Hertzsprung-Russell diagram matches with the $M_{\text{ini}} = 25M_{\odot}$ MIST evolutionary models within the last 10^4 yr before the end of its life. This work reveals [W60] B90 as the perfect laboratory to study episodic mass loss in evolved RSGs at low- Z environments. Despite our detailed analysis, further investigation is needed to shed more light on the system. Observations with high spatial resolution, i.e. ALMA or VLTI, are needed to resolve the CSM structures and visually identify the speculated bow shock. Additionally, the coronagraph mounted on the *James Webb* Space Telescope would allow us to resolve the closest environment revealing the distribution of the warm dust formed by prior mass ejections. We propose to extend a similar analysis to other very luminous RSGs (e.g. WOH G64, RSGs in low- Z galaxies from the ASSESS project; Levesque et al. 2009; de Wit et al. 2024) to understand their properties and check the similarities with respect to [W60] B90. Constraining the behavior of the most luminous RSGs is crucial to understanding their evolution, as well as the ‘RSG problem’, and the origin of the observed upper L limit of RSGs.

Acknowledgements. GMS, SdW, AZB, KA, EC, and MK acknowledge funding support from the European Research Council (ERC) under the European Union’s Horizon 2020 research and innovation programme (Grant agreement No. 772086). The work of KB is supported by NOIRLab, which is managed by the Association of Universities for Research in Astronomy (AURA) under a cooperative agreement with the U.S. National Science Foundation. We acknowledge useful discussions with Grigoris Maravelias, Manos Zapartas, Despina Hatzidimitriou, Stavros Akras, Maria Kopsacheili, and Maria del Mar Rubio. This paper includes data gathered with the 6.5m Magellan Telescopes located at Las Campanas Observatory, Chile. This research is based on observations made with the NASA/ESA Hubble Space Telescope obtained from the Space Telescope Science Institute, which is operated by the Association of Universities for Research in Astronomy, Inc., under NASA contract NAS 5–26555. These observations are associated with program 10583. This work is based in part on observations made with the *Spitzer* Space Telescope, which is operated by the Jet Propulsion Laboratory, California Institute of Technology under a contract with NASA. This work has made use of data from the European Space Agency (ESA) mission *Gaia* (<https://www.cosmos.esa.int/gaia>), processed by the *Gaia* Data Processing and Analysis Consortium (DPAC, <https://www.cosmos.esa.int/web/gaia/dpac/consortium>). Funding for the DPAC has been provided by national institutions, in particular the institutions participating in the *Gaia* Multilateral Agreement. This publication makes use of data products from the Near-Earth Object Wide-field Infrared Survey Explorer (NEOWISE), which is a joint project of the Jet Propulsion Laboratory/California

Institute of Technology and the University of Arizona. NEOWISE is funded by the National Aeronautics and Space Administration. This work has made use of data from the Asteroid Terrestrial-impact Last Alert System (ATLAS) project. The Asteroid Terrestrial-impact Last Alert System (ATLAS) project is primarily funded to search for near earth asteroids through NASA grants NN12AR55G, 80NSSC18K0284, and 80NSSC18K1575; byproducts of the NEO search include images and catalogs from the survey area. This work was partially funded by Kepler/K2 grant J1944/80NSSC19K0112 and HST GO-15889, and STFC grants ST/T000198/1 and ST/S006109/1. The ATLAS science products have been made possible through the contributions of the University of Hawaii Institute for Astronomy, the Queen’s University Belfast, the Space Telescope Science Institute, the South African Astronomical Observatory, and The Millennium Institute of Astrophysics (MAS), Chile. We acknowledge with thanks the variable star observations from the AAVSO International Database contributed by observers worldwide and used in this research. This research made use of Astropy⁵, a community-developed core Python package for Astronomy (Astropy Collaboration et al. 2013, 2018).

References

- Adams, S. M., Kochanek, C. S., Gerke, J. R., et al. 2017, MNRAS, 468, 4968
Alcock, C., Allsman, R. A., Alves, D., et al. 1997, ApJ, 486, 697
Alcock, C., Allsman, R. A., Alves, D. R., et al. 1999, PASP, 111, 1539
Antoniadis, K., Bonanos, A. Z., de Wit, S., et al. 2024, A&A, in press, (arXiv:2401.15163)
Anugu, N., Baron, F., Gies, D. R., et al. 2023, AJ, 166, 78
Astropy Collaboration, Price-Whelan, A. M., Sipőcz, B. M., et al. 2018, AJ, 156, 123
Astropy Collaboration, Robitaille, T. P., Tollerud, E. J., et al. 2013, A&A, 558, A33
Bergemann, M., Kudritzki, R.-P., Gazak, Z., et al. 2015, ApJ, 804, 113
Bergemann, M., Kudritzki, R.-P., Plez, B., et al. 2012, ApJ, 751, 156
Bergemann, M., Kudritzki, R.-P., Würl, M., et al. 2013, ApJ, 764, 115
Bonanos, A. Z., Trammer, F., de Wit, S., et al. 2023, A&A, in press, (arXiv:2312.04626)
Chatys, F. W., Bedding, T. R., Murphy, S. J., et al. 2019, MNRAS, 487, 4832
Choi, J., Dotter, A., Conroy, C., et al. 2016, ApJ, 823, 102
Cox, N. L. J., Kerschbaum, F., van Marle, A. J., et al. 2012, A&A, 537, A35
Cutri, R. M., Wright, E. L., Conrow, T., et al. 2021, VizieR Online Data Catalog, II/328
Davies, B., Crowther, P. A., & Beasor, E. R. 2018, MNRAS, 478, 3138
Davies, B., Kudritzki, R.-P., Gazak, Z., et al. 2015, ApJ, 806, 21
Davies, B., Kudritzki, R.-P., Plez, B., et al. 2013, ApJ, 767, 3
Davies, B. & Plez, B. 2021, MNRAS, 508, 5757
de Jager, C., Nieuwenhuijzen, H., & van der Hucht, K. A. 1988, A&AS, 72, 259
de Wit, S., Bonanos, A. Z., Antoniadis, K., et al. 2024, A&A, in press, (arXiv:2402.12442)
de Wit, S., Bonanos, A. Z., Trammer, F., et al. 2023, A&A, 669, A86
Decin, L., Cox, N. L. J., Royer, P., et al. 2012, A&A, 548, A113
Decin, L., Hony, S., de Koter, A., et al. 2006, A&A, 456, 549
Dorda, R., Negueruela, I., González-Fernández, C., & Tabernero, H. M. 2016, A&A, 592, A16
Dorda, R. & Patrick, L. R. 2021, MNRAS, 502, 4890
Dotter, A. 2016, ApJS, 222, 8

⁵ <http://www.astropy.org>

- Drevon, J., Millour, F., Cruzalèbes, P., et al. 2024, *MNRAS*, 527, L88
- Dupree, A. K., Strassmeier, K. G., Calderwood, T., et al. 2022, *ApJ*, 936, 18
- Ekström, S., Georgy, C., Eggenberger, P., et al. 2012, *A&A*, 537, A146
- Fraser, O. J., Hawley, S. L., & Cook, K. H. 2008, *AJ*, 136, 1242
- Gaia Collaboration, Prusti, T., de Bruijne, J. H. J., et al. 2016, *A&A*, 595, A1
- Gaia Collaboration, Vallenari, A., Brown, A. G. A., et al. 2023, *A&A*, 674, A1
- González-Torà, G., Wittkowski, M., Davies, B., & Plez, B. 2023, *A&A*, in press, (arXiv:2312.12521)
- Gordon, K. D., Clayton, G. C., Misselt, K. A., Landolt, A. U., & Wolff, M. J. 2003, *ApJ*, 594, 279
- Groenewegen, M. A. T. & Sloan, G. C. 2018, *A&A*, 609, A114
- Groenewegen, M. A. T., Sloan, G. C., Soszyński, I., & Petersen, E. A. 2009, *A&A*, 506, 1277
- Gvaramadze, V. V., Menten, K. M., Kniazev, A. Y., et al. 2014, *MNRAS*, 437, 843
- Harper, G. M., Brown, A., & Guinan, E. F. 2008, *AJ*, 135, 1430
- Harper, G. M., Brown, A., Guinan, E. F., et al. 2017, *AJ*, 154, 11
- Heinze, A. N., Tonry, J. L., Denneau, L., et al. 2018, *AJ*, 156, 241
- Henize, K. G. 1956, *ApJS*, 2, 315
- Hollis, J. M., Oliverson, R. J., Wagner, R. M., & Feibelman, W. A. 1992, *ApJ*, 393, 217
- Houck, J. R., Roellig, T. L., Van Cleve, J., et al. 2004, in *Society of Photo-Optical Instrumentation Engineers (SPIE) Conference Series*, Vol. 5487, *Optical, Infrared, and Millimeter Space Telescopes*, ed. J. C. Mather, 62–76
- Jayasinghe, T., Kochanek, C. S., Stanek, K. Z., et al. 2018, *MNRAS*, 477, 3145
- Jiménez-Arranz, Ó., Romero-Gómez, M., Luri, X., et al. 2023, *A&A*, 669, A91
- Jones, O. C., Kemper, F., Sargent, B. A., et al. 2012, *MNRAS*, 427, 3209
- Jones, T. J., Shenoy, D., & Humphreys, R. 2023, *Research Notes of the American Astronomical Society*, 7, 92
- Josselin, E. & Plez, B. 2007, *A&A*, 469, 671
- Joyce, M., Leung, S.-C., Molnár, L., et al. 2020, *ApJ*, 902, 63
- Kaper, L., van Loon, J. T., Augusteijn, T., et al. 1997, *ApJ*, 475, L37
- Kelson, D. D. 2003, *PASP*, 115, 688
- Kelson, D. D., Illingworth, G. D., van Dokkum, P. G., & Franx, M. 2000, *ApJ*, 531, 159
- Kiss, L. L., Szabó, G. M., & Bedding, T. R. 2006, *MNRAS*, 372, 1721
- Kochanek, C. S., Shappee, B. J., Stanek, K. Z., et al. 2017, *PASP*, 129, 104502
- Kopsacheili, M., Zezas, A., & Leonidaki, I. 2020, *MNRAS*, 491, 889
- Kravchenko, K., Chiavassa, A., Van Eck, S., et al. 2019, *A&A*, 632, A28
- Kravchenko, K., Jorissen, A., Van Eck, S., et al. 2021, *A&A*, 650, L17
- Laplace, E., Göteborg, Y., de Mink, S. E., Justham, S., & Farmer, R. 2020, *A&A*, 637, A6
- Le Bertre, T., Matthews, L. D., Gérard, E., & Libert, Y. 2012, *MNRAS*, 422, 3433
- Levesque, E. M. 2017, *Astrophysics of Red Supergiants*
- Levesque, E. M., Massey, P., Olsen, K. A. G., & Plez, B. 2007, *ApJ*, 667, 202
- Levesque, E. M., Massey, P., Olsen, K. A. G., et al. 2005, *ApJ*, 628, 973
- Levesque, E. M., Massey, P., Plez, B., & Olsen, K. A. G. 2009, *AJ*, 137, 4744
- Luridiana, V., Morisset, C., & Shaw, R. A. 2015, *A&A*, 573, A42
- Ma, J.-Z., Chiavassa, A., de Mink, S. E., et al. 2024, *ApJ*, 962, L36
- Mackey, J., Mohamed, S., Neilson, H. R., Langer, N., & Meyer, D. M. A. 2012, *ApJ*, 751, L10
- MacLeod, M., Antoni, A., Huang, C. D., et al. 2023, *ApJ*, 956, 27
- Mainzer, A., Bauer, J., Cutri, R. M., et al. 2014, *ApJ*, 792, 30
- Mainzer, A., Bauer, J., Grav, T., et al. 2011, *ApJ*, 731, 53
- Marshall, J. L., Bures, S., Thompson, I. B., et al. 2008, in *Ground-based and Airborne Instrumentation for Astronomy II*, ed. I. S. McLean & M. M. Casali, Vol. 7014, *International Society for Optics and Photonics (SPIE)*, 701454
- Mathewson, D. S. & Clarke, J. N. 1973, *ApJ*, 180, 725
- Meixner, M., Gordon, K. D., Indebetouw, R., et al. 2006, *AJ*, 132, 2268
- Meyer, D. M. A., Mignone, A., Petrov, M., et al. 2021, *MNRAS*, 506, 5170
- Meynet, G., Georgy, C., Hirschi, R., et al. 2011, *Bulletin de la Societe Royale des Sciences de Liege*, 80, 266
- Montargès, M., Cannon, E., Lagarde, E., et al. 2021, *Nature*, 594, 365
- Noriega-Crespo, A., van Buren, D., Cao, Y., & Dgani, R. 1997a, *AJ*, 114, 837
- Noriega-Crespo, A., van Buren, D., & Dgani, R. 1997b, *AJ*, 113, 780
- Osterbrock, D. E. 1989, *Astrophysics of gaseous nebulae and active galactic nuclei*
- Patrick, L. R. 2020, in *XIV.0 Scientific Meeting (virtual) of the Spanish Astronomical Society*, 174
- Patrick, L. R., Evans, C. J., Davies, B., et al. 2017, *MNRAS*, 468, 492
- Patrick, L. R., Thilker, D., Lennon, D. J., et al. 2022, *MNRAS*, 513, 5847
- Pietrzyński, G., Graczyk, D., Galle, A., et al. 2019, *Nature*, 567, 200
- Pojmanski, G. 1997, *Acta Astron.*, 47, 467
- Renzo, M., Zapartas, E., de Mink, S. E., et al. 2019, *A&A*, 624, A66
- Riebel, D., Boyer, M. L., Srinivasan, S., et al. 2015, *ApJ*, 807, 1
- Riebel, D., Srinivasan, S., Sargent, B., & Meixner, M. 2012, *ApJ*, 753, 71
- Shappee, B. J., Prieto, J. L., Grupe, D., et al. 2014, *ApJ*, 788, 48
- Shingles, L., Smith, K. W., Young, D. R., et al. 2021, *Transient Name Server AstroNote*, 7, 1
- Smartt, S. J. 2009, *ARA&A*, 47, 63
- Smartt, S. J. 2015, *PASA*, 32, e016
- Smartt, S. J., Eldridge, J. J., Crockett, R. M., & Maund, J. R. 2009, *MNRAS*, 395, 1409
- Stoop, M., Kaper, L., de Koter, A., et al. 2023, *A&A*, 670, A108
- Sukhbold, T., Ertl, T., Woosley, S. E., Brown, J. M., & Janka, H. T. 2016, *ApJ*, 821, 38
- Taberner, H. M., Dorda, R., Negueruela, I., & González-Fernández, C. 2018, *MNRAS*, 476, 3106
- Tetzlaff, N., Neuhäuser, R., & Hohle, M. M. 2011, *MNRAS*, 410, 190
- Tonry, J. L., Denneau, L., Heinze, A. N., et al. 2018, *PASP*, 130, 064505
- Udalski, A., Kubiak, M., & Szymanski, M. 1997, *Acta Astron.*, 47, 319
- Udalski, A., Soszynski, I., Szymanski, M. K., et al. 2008, *Acta Astron.*, 58, 89
- Udalski, A., Szymański, M. K., & Szymański, G. 2015, *Acta Astron.*, 65, 1
- Ulaczyk, K., Szymański, M. K., Udalski, A., et al. 2013, *Acta Astron.*, 63, 159
- van Loon, J. T., Cioni, M. R. L., Zijlstra, A. A., & Loup, C. 2005, *A&A*, 438, 273
- Walborn, N. R. & Fitzpatrick, E. L. 1990, *PASP*, 102, 379
- Watson, C. L., Henden, A. A., & Price, A. 2006, *Society for Astronomical Sciences Annual Symposium*, 25, 47
- Wheeler, J. C. & Chatzopoulos, E. 2023, *Astronomy and Geophysics*, 64, 3.11
- Wright, E. L., Eisenhardt, P. R. M., Mainzer, A. K., et al. 2010, *AJ*, 140, 1868
- Yang, M., Bonanos, A. Z., Jiang, B., et al. 2021, *A&A*, 646, A141
- Yang, M., Bonanos, A. Z., Jiang, B., et al. 2023, *A&A*, 676, A84
- Yang, M., Bonanos, A. Z., Jiang, B.-W., et al. 2018, *A&A*, 616, A175
- Yang, M. & Jiang, B. W. 2011, *ApJ*, 727, 53

Appendix A: Local proper motion values

Table A.1: Local proper motion of [W60] B90

Cone size		N_{Gaia}	P_{LMC}	N_{clean}	pm_{RA}	pm_{DEC}	v
(')	(pc)				(mas yr ⁻¹)	(mas yr ⁻¹)	(km s ⁻¹)
36	520	1320847	0.9	329739	0.0621	0.0212	16 ⁺¹² ₋₁₀
			0.7	372327	0.0618	0.0231	16 ⁺¹² ₋₁₀
			0.5	394645	0.0601	0.0268	16 ⁺¹¹ ₋₁₀
18	260	360395	0.9	83522	0.0606	0.0322	16 ⁺¹² ₋₁₁
			0.7	95011	0.0623	0.0290	16 ⁺¹² ₋₁₀
			0.5	101062	0.0622	0.0267	16 ⁺¹² ₋₁₀
6	87	40737	0.9	9009	0.0643	0.0312	17 ⁺¹² ₋₁₁
			0.7	10297	0.0712	0.0259	18 ⁺¹¹ ₋₁₀
			0.5	10976	0.0703	0.0224	17 ⁺¹¹ ₋₁₀
4.5	65	22824	0.9	5075	0.0657	0.0264	17 ⁺¹² ₋₁₀
			0.7	5810	0.0699	0.0220	17 ⁺¹¹ ₋₁₀
			0.5	6201	0.0712	0.0179	17 ⁺¹¹ ₋₉
3	43	10145	0.9	2261	0.0672	0.0096	16 ⁺¹¹ ₋₉
			0.7	2605	0.0712	0.0070	17 ⁺¹¹ ₋₉
			0.5	2788	0.0757	0.0053	18 ⁺¹⁰ ₋₉
2.4	35	6586	0.9	1458	0.0849	0.0137	20 ⁺¹¹ ₋₉
			0.7	1684	0.0859	0.0155	21 ⁺¹¹ ₋₉
			0.5	1807	0.0928	0.0146	22 ⁺¹¹ ₋₉
1.8	26	3758	0.9	830	0.0857	0.0356	22 ⁺¹² ₋₁₁
			0.7	959	0.0896	0.0394	23 ⁺¹² ₋₁₁
			0.5	1031	0.0964	0.0390	25 ⁺¹¹ ₋₁₁

Notes. Proper motion error of [W60] B90 from *Gaia* DR3: $\sigma_{pm,RA} = 0.0374$ mas yr⁻¹, $\sigma_{pm,DEC} = 0.0343$ mas yr⁻¹.

Appendix B: Apertures and fluxes measured

Table B.1: Position of each aperture subtracted to inspect the nebular emission

Name	RA (J2000)	Dec. (J2000)	Name	RA (J2000)	Dec. (J2000)
Epoch2a	05:24:18.99	-69:38:54.1	Neb4a	05:24:20.33	-69:38:48.4
Epoch2b	05:24:19.11	-69:38:52.2	Neb4b	05:24:20.00	-69:38:47.8
Epoch2c	05:24:19.08	-69:38:48.9	Neb4c	05:24:19.62	-69:38:47.1
Epoch2d	05:24:19.40	-69:38:47.3	Neb4d	05:24:19.41	-69:38:46.7
Epoch3a	05:24:20.12	-69:38:49.3	Neb4e	05:24:19.19	-69:38:46.3
Epoch3b	05:24:19.72	-69:38:49.3	Neb4f	05:24:18.93	-69:38:45.8
Epoch3c	05:24:18.91	-69:38:49.3	Neb5a	05:24:20.13	-69:38:47.4
Epoch3d	05:24:18.52	-69:38:49.3	Neb5b	05:24:20.10	-69:38:48.6
Neb1a	05:24:19.84	-69:38:48.7	Neb5c	05:24:20.03	-69:38:51.0
Neb1b	05:24:19.96	-69:38:48.6	Neb5d	05:24:20.00	-69:38:52.5
Neb1c	05:24:20.24	-69:38:48.3	Neb5e	05:24:20.11	-69:38:48.7
Neb1d	05:24:20.57	-69:38:47.8	Neb6a	05:24:19.80	-69:38:42.7
Neb1e	05:24:20.91	-69:38:47.4	Neb6b	05:24:19.94	-69:38:45.0
Neb2a	05:24:19.43	-69:38:46.1	Neb6c	05:24:19.93	-69:38:45.0
Neb2b	05:24:19.72	-69:38:47.0	Neb6d	05:24:20.13	-69:38:48.6
Neb2c	05:24:20.41	-69:38:49.2			
Neb3a	05:24:19.39	-69:38:45.6			
Neb3b	05:24:19.66	-69:38:45.2			
Neb3c	05:24:19.88	-69:38:44.8			
Neb3d	05:24:20.65	-69:38:43.6			

Table B.2: Emission line fluxes measured in each aperture presented in B.1. Wavelengths are in Å, flux H β in ergs cm⁻²s⁻¹Å⁻¹ and RV in km s⁻¹

Line	λ_{obs}	Epoch2a				Epoch2b				
		F_{obs}	F_{corr}	S/N	RV	λ_{obs}	F_{obs}	F_{corr}	S/N	RV
[O II] 3726	-	-	-	-	-	-	-	-	-	-
[O II] 3729	-	-	-	-	-	-	-	-	-	-
H γ 4341	-	-	-	-	-	-	-	-	-	-
H β 4861	4865.82	100	100	8	275	4865.78	100	100	7	273
[O III] 5007	-	-	-	-	-	-	-	-	-	-
[O I] 6300	-	-	-	-	-	6306.88	46	33	3	311
[N II] 6527	6533.02	36	37	3	264	-	-	-	-	-
[N II] 6548	-	-	-	-	-	6553.90	41	27	4	266
H α 6563	6568.83	278	286	25	274	6568.79	427	287	25	272
[N II] 6584	-	-	-	-	-	6589.62	82	55	5	279
[S II] 6716	6722.78	63	65	10	281	6722.72	92	60	6	278
[S II] 6731	6737.25	31	32	20	285	6737.17	72	47	5	281
$F_{\text{H}\beta}$		2.20					1.52			
$c(\text{H}\beta)$		0.00 $^{+0.23}_{-0.00}$					0.54 \pm 0.26			
$E(B - V)$		0.03 $^{+0.16}_{-0.00}$					0.38 \pm 0.18			
[S II]/H α		0.34 \pm 0.04					0.37 \pm 0.08			
[N II]/H α		-					0.19 \pm 0.04			
[O I]/H α		-					0.11 \pm 0.04			
[O II]/H β		-					-			
[O III]/H β		-					-			

Line	λ_{obs}	Epoch2e				Epoch2d				
		F_{obs}	F_{corr}	S/N	RV	λ_{obs}	F_{obs}	F_{corr}	S/N	RV
[O II] 3726	-	-	-	-	-	-	-	-	-	-
[O II] 3729	-	-	-	-	-	-	-	-	-	-
H γ 4341	-	-	-	-	-	4344.54	30	39	4	280
H β 4861	4865.62	100	100	6	263	4865.77	100	100	20	272
[O III] 5007	-	-	-	-	-	5011.61	23	22	4	283
[O I] 6300	6306.72	103	76	10	303	6306.65	36	22	12	300
[N II] 6527	-	-	-	-	-	-	-	-	-	-
[N II] 6548	6553.69	71	50	7	257	6553.92	39	22	7	267
H α 6563	6568.88	409	287	25	276	6568.82	507	286	25	273
[N II] 6584	-	-	-	-	-	6589.57	99	56	20	276
[S II] 6716	6722.97	84	58	8	290	6722.83	133	72	33	283
[S II] 6731	6737.28	57	39	5	286	6737.19	98	53	33	282
$F_{\text{H}\beta}$		1.50					4.20			
$c(\text{H}\beta)$		0.48 \pm 0.29					0.78 \pm 0.12			
$E(B - V)$		0.34 \pm 0.20					0.54 \pm 0.09			
[S II]/H α		0.34 \pm 0.06					0.44 \pm 0.03			
[N II]/H α		-					0.19 \pm 0.02			
[O I]/H α		0.26 \pm 0.04					0.08 \pm 0.01			
[O II]/H β		-					-			
[O III]/H β		-					0.22 \pm 0.06			

Line	Epoch3a					Epoch3b				
	λ_{obs}	F_{obs}	F_{corr}	S/N	RV	λ_{obs}	F_{obs}	F_{corr}	S/N	RV
[O II] 3726	-	-	-	-	-	-	-	-	-	-
[O II] 3729	-	-	-	-	-	3732.24	161	222	3	278
H γ 4341	-	-	-	-	-	-	-	-	-	-
H β 4861	4865.64	100	100	10	268	4865.73	100	100	10	274
[O III] 5007	5011.34	42	39	6	271	-	-	-	-	-
[O I] 6300	6306.83	59	35	8	313	6306.84	38	28	5	313
[N II] 6527	-	-	-	-	-	-	-	-	-	-
[N II] 6548	6553.75	61	34	6	264	6553.83	73	52	7	267
H α 6563	6568.74	514	285	25	274	6568.8	402	286	25	276
[N II] 6584	6589.51	99	55	10	278	6589.29	49	35	5	268
[S II] 6716	6722.76	150	80	25	284	6722.92	75	52	7	291
[S II] 6731	6737.15	96	51	25	285	6737.10	69	48	7	282
$F_{\text{H}\beta}$	1.66					1.57				
$c(\text{H}\beta)$	0.80 ± 0.20					0.46 ± 0.2				
$E(B - V)$	0.56 ± 0.14					0.32 ± 0.14				
[S II]/H α	0.46 ± 0.04					0.35 ± 0.06				
[N II]/H α	0.19 ± 0.03					0.12 ± 0.03				
[O I]/H α	0.12 ± 0.02					0.10 ± 0.02				
[O II]/H β	-					-				
[O III]/H β	0.39 ± 0.10					-				
Line	Epoch3c					Epoch3d				
	λ_{obs}	F_{obs}	F_{corr}	S/N	RV	λ_{obs}	F_{obs}	F_{corr}	S/N	RV
[O II] 3726	-	-	-	-	-	-	-	-	-	-
[O II] 3729	-	-	-	-	-	-	-	-	-	-
H γ 4341	-	-	-	-	-	-	-	-	-	-
H β 4861	4865.79	100	100	7	278	4865.71	100	100	7	273
[O III] 5007	-	-	-	-	-	-	-	-	-	-
[O I] 6300	6306.95	93	58	5	318	6306.8	74	38	5	311
[N II] 6527	6533.29	81	48	5	280	6532.86	39	18	3	260
[N II] 6548	6553.90	123	72	7	270	6553.86	110	51	9	269
H α 6563	6568.69	489	286	25	271	6568.76	617	287	25	274
[N II] 6584	6589.45	51	30	3	275	6589.54	94	44	8	279
[S II] 6716	6722.52	108	61	7	274	6722.70	132	58	14	282
[S II] 6731	6737.22	56	31	4	288	6737.14	91	40	10	284
$F_{\text{H}\beta}$	0.88					0.90				
$c(\text{H}\beta)$	0.73 ± 0.26					1.04 ± 0.24				
$E(B - V)$	0.51 ± 0.18					0.73 ± 0.17				
[S II]/H α	0.32 ± 0.07					0.34 ± 0.04				
[N II]/H α	0.10 ± 0.04					0.15 ± 0.02				
[O I]/H α	0.20 ± 0.05					0.13 ± 0.03				
[O II]/H β	-					-				
[O III]/H β	-					-				

Line	Neb1a					Neb1b						
	λ_{obs}	F_{obs}	F_{corr}	S/N	RV	λ_{obs}	F_{obs}	F_{corr}	S/N	RV		
[O II] 3726	3729.4	120	170	5	273	3729.36	152	222	8	270		
[O II] 3729	3732.14	167	235	7	269	3732.15	153	222	8	270		
H γ 4341	4344.51	44	51	4	281	4344.45	33	39	3	277		
H β 4861	4865.78	100	100	12	277	4865.83	100	100	14	280		
[O III] 5007	-	-	-	-	-	5011.28	26	25	5	267		
[O I] 6300	6306.95	43	31	5	318	6306.81	44	31	7	311		
[N II] 6527	-	-	-	-	-	6532.92	21	14	9	263		
[N II] 6548	6553.70	47	33	5	261	6553.77	62	42	6	264		
H α 6563	6568.79	411	286	25	275	6568.84	422	286	25	278		
[N II] 6584	6589.49	59	41	7	276	6589.51	89	60	25	277		
[S II] 6716	6722.71	100	68	14	282	6722.72	112	74	33	282		
[S II] 6731	6737.08	83	56	11	281	6737.17	76	50	20	285		
$F_{\text{H}\beta}$		2.09						2.08				
$c(\text{H}\beta)$		0.49 ± 0.17						0.53 ± 0.15				
$E(B - V)$		0.34 ± 0.12						0.37 ± 0.11				
[S II]/H α		0.44 ± 0.05						0.43 ± 0.03				
[N II]/H α		0.14 ± 0.02						0.21 ± 0.02				
[O I]/H α		0.11 ± 0.02						0.11 ± 0.02				
[O II]/H β		4.05 ± 0.99						4.44 ± 0.84				
[O III]/H β		-						0.25 ± 0.07				

Line	Neb1c					Neb1d						
	λ_{obs}	F_{obs}	F_{corr}	S/N	RV	λ_{obs}	F_{obs}	F_{corr}	S/N	RV		
[O II] 3726	3729.39	107	138	7	272	3729.35	116	136	5	269		
[O II] 3729	3732.20	150	194	11	274	3732.18	150	175	6	272		
H γ 4341	4344.50	23	26	3	281	-	-	-	-	-		
H β 4861	4865.82	100	100	14	279	4865.79	100	100	14	277		
[O III] 5007	5011.32	25	25	7	270	5011.34	36	35	6	271		
[O I] 6300	6306.78	28	22	5	310	6306.92	36	31	5	317		
[N II] 6527	6533.02	19	15	5	267	6532.92	23	20	5	263		
[N II] 6548	6553.75	43	33	11	263	6553.62	36	31	9	257		
H α 6563	6568.82	372	286	25	277	6568.81	338	287	25	276		
[N II] 6584	6589.53	74	57	33	278	6589.56	43	37	14	280		
[S II] 6716	6722.77	94	71	33	284	6722.77	78	65	25	284		
[S II] 6731	6737.18	70	53	33	286	6737.26	57	48	20	289		
$F_{\text{H}\beta}$		2.60						2.00				
$c(\text{H}\beta)$		0.36 ± 0.15						0.22 ± 0.15				
$E(B - V)$		0.25 ± 0.11						0.16 ± 0.11				
[S II]/H α		0.43 ± 0.03						0.39 ± 0.03				
[N II]/H α		0.20 ± 0.01						0.13 ± 0.01				
[O I]/H α		0.08 ± 0.02						0.11 ± 0.02				
[O II]/H β		3.32 ± 0.59						3.11 ± 0.74				
[O III]/H β		0.25 ± 0.05						0.35 ± 0.08				

Line	Neb1e					Neb2a				
	λ_{obs}	F_{obs}	F_{corr}	S/N	RV	λ_{obs}	F_{obs}	F_{corr}	S/N	RV
[O II] 3726	3729.36	190	254	5	270	3729.44	134	150	10	276
[O II] 3729	3732.20	176	234	5	274	3732.19	151	169	10	273
H γ 4341	-	-	-	-	-	4344.64	42	44	5	290
H β 4861	4865.73	100	100	8	273	4865.78	100	100	25	277
[O III] 5007	5011.35	41	40	5	272	5011.56	20	20	6	284
[O I] 6300	6306.77	55	42	6	309	6306.65	24	22	10	304
[N II] 6527	6533.00	38	28	6	266	6532.99	11	9	6	266
[N II] 6548	6553.82	63	47	10	266	6553.78	27	24	14	265
H α 6563	6568.76	387	286	25	274	6568.80	322	287	25	276
[N II] 6584	6589.48	60	44	10	276	6589.58	44	39	25	280
[S II] 6716	6722.68	92	66	20	280	6722.82	75	66	33	287
[S II] 6731	6737.16	52	38	11	285	6737.17	53	47	33	285
$F_{\text{H}\beta}$	1.19					3.94				
$c(\text{H}\beta)$	0.41 ± 0.23					0.16 ± 0.11				
$E(B - V)$	0.29 ± 0.16					0.11 ± 0.08				
[S II]/H α	0.36 ± 0.04					0.39 ± 0.03				
[N II]/H α	0.15 ± 0.02					0.14 ± 0.01				
[O I]/H α	0.15 ± 0.03					0.08 ± 0.01				
[O II]/H β	4.88 ± 1.54					3.19 ± 0.45				
[O III]/H β	0.40 ± 0.12					0.20 ± 0.04				

Line	Neb2b					Neb2c				
	λ_{obs}	F_{obs}	F_{corr}	S/N	RV	λ_{obs}	F_{obs}	F_{corr}	S/N	RV
[O II] 3726	3729.41	66	81	4	274	3729.46	94	110	3	278
[O II] 3729	3732.18	107	131	7	272	3732.17	124	144	3	272
H γ 4341	4344.62	34	37	4	289	-	-	-	-	-
H β 4861	4865.77	100	100	25	276	4865.72	100	100	12	273
[O III] 5007	5011.43	18	18	8	276	-	-	-	-	-
[O I] 6300	6306.54	29	24	11	299	6306.81	37	32	7	311
[N II] 6527	6533.07	11	9	5	270	6533.15	22	19	4	273
[N II] 6548	6553.87	39	32	20	269	6553.63	58	50	11	258
H α 6563	6568.85	355	287	25	278	6568.79	334	287	25	275
[N II] 6584	6589.56	59	48	20	280	6589.52	42	36	10	278
[S II] 6716	6722.86	93	74	25	288	6722.73	76	65	25	283
[S II] 6731	6737.22	70	56	25	287	6737.28	62	53	25	290
$F_{\text{H}\beta}$	3.94					2.00				
$c(\text{H}\beta)$	0.29 ± 0.11					0.21 ± 0.17				
$E(B - V)$	0.21 ± 0.08					0.15 ± 0.12				
[S II]/H α	0.45 ± 0.04					0.41 ± 0.03				
[N II]/H α	0.17 ± 0.02					0.13 ± 0.02				
[O I]/H α	0.08 ± 0.01					0.11 ± 0.02				
[O II]/H β	2.12 ± 0.45					2.53 ± 0.97				
[O III]/H β	0.18 ± 0.03					-				

Line	Neb3a					Neb3b				
	λ_{obs}	F_{obs}	F_{corr}	S/N	RV	λ_{obs}	F_{obs}	F_{corr}	S/N	RV
[O II] 3726	3729.41	111	131	5	274	3729.40	99	115	4	273
[O II] 3729	3732.22	106	125	5	276	3732.17	98	113	4	272
H γ 4341	4344.68	40	43	6	293	4344.69	42	45	5	294
H β 4861	4865.77	100	100	20	276	4865.75	100	100	25	275
[O III] 5007	5011.36	23	23	7	272	5011.46	22	21	7	278
[O I] 6300	6306.84	30	26	10	313	6306.82	25	22	10	312
[N II] 6527	6533.03	13	11	7	268	6533.19	13	11	9	275
[N II] 6548	6553.79	29	25	16	265	6553.75	21	18	14	263
H α 6563	6568.81	338	286	25	276	6568.80	333	286	25	276
[N II] 6584	6589.55	27	23	14	279	6589.55	21	18	12	279
[S II] 6716	6722.83	57	47	33	287	6722.80	53	45	33	286
[S II] 6731	6737.27	41	34	33	290	6737.15	35	30	25	284
$F_{\text{H}\beta}$		3.43				3.21				
$c(\text{H}\beta)$		0.23 ± 0.12				0.21 ± 0.11				
$E(B - V)$		0.16 ± 0.09				0.15 ± 0.08				
[S II]/H α		0.29 ± 0.02				0.26 ± 0.02				
[N II]/H α		0.08 ± 0.01				0.06 ± 0.01				
[O I]/H α		0.09 ± 0.01				0.08 ± 0.01				
[O II]/H β		2.56 ± 0.60				2.28 ± 0.64				
[O III]/H β		0.23 ± 0.04				0.21 ± 0.04				

Line	Neb3c					Neb3d				
	λ_{obs}	F_{obs}	F_{corr}	S/N	RV	λ_{obs}	F_{obs}	F_{corr}	S/N	RV
[O II] 3726	3729.44	130	146	5	276	3729.54	244	269	5	284
[O II] 3729	3732.21	128	143	5	275	3732.22	289	318	6	276
H γ 4341	4344.58	41	43	3	286	-	-	-	-	-
H β 4861	4865.74	100	100	25	274	4865.76	100	100	10	275
[O III] 5007	5011.33	17	17	5	270	5011.37	46	46	5	273
[O I] 6300	6306.82	26	23	10	312	6306.82	64	58	9	312
[N II] 6527	6533.24	13	12	7	277	6532.85	38	34	10	259
[N II] 6548	6553.73	30	26	16	262	6553.80	50	45	14	265
H α 6563	6568.88	321	286	25	280	6568.82	318	287	25	277
[N II] 6584	6589.59	19	17	10	281	6589.65	46	42	12	284
[S II] 6716	6722.92	48	42	33	291	6722.81	70	63	25	286
[S II] 6731	6737.27	38	33	33	290	6737.24	58	52	20	288
$F_{\text{H}\beta}$		3.10				1.49				
$c(\text{H}\beta)$		0.16 ± 0.11				$0.14^{+0.20}_{-0.14}$				
$E(B - V)$		0.11 ± 0.08				$0.10^{+0.14}_{-0.10}$				
[S II]/H α		0.26 ± 0.02				0.40 ± 0.03				
[N II]/H α		0.06 ± 0.01				0.15 ± 0.02				
[O I]/H α		0.08 ± 0.01				0.20 ± 0.03				
[O II]/H β		2.89 ± 0.64				5.87 ± 1.61				
[O III]/H β		0.17 ± 0.04				0.46 ± 0.14				

Line	Neb4a					Neb4b				
	λ_{obs}	F_{obs}	F_{corr}	S/N	RV	λ_{obs}	F_{obs}	F_{corr}	S/N	RV
[O II] 3726	-	-	-	-	-	3729.30	79	141	3	261
[O II] 3729	-	-	-	-	-	3732.17	187	333	6	268
H γ 4341	-	-	-	-	-	4344.49	39	50	5	276
H β 4861	4865.83	100	100	16	276	4865.83	100	100	25	276
[O III] 5007	5011.61	62	58	9	283	5011.51	45	42	9	277
[O I] 6300	6306.71	45	25	6	303	6306.85	48	28	11	310
[N II] 6527	6533.15	39	20	7	269	-	-	-	-	-
[N II] 6548	6553.71	56	28	10	258	6553.83	62	34	12	263
H α 6563	6568.83	582	287	25	273	6568.85	524	286	25	274
[N II] 6584	6589.47	69	34	12	272	6589.53	70	38	14	274
[S II] 6716	6722.79	195	92	33	281	6722.84	194	102	33	284
[S II] 6731	6737.17	131	61	33	281	6737.25	124	65	33	285
$F_{\text{H}\beta}$	1.65					2.33				
$c(\text{H}\beta)$	0.96 ± 0.14					0.82 ± 0.11				
$E(B - V)$	0.67 ± 0.10					0.57 ± 0.08				
[S II]/H α	0.53 ± 0.04					0.58 ± 0.04				
[N II]/H α	0.12 ± 0.01					0.13 ± 0.01				
[O I]/H α	0.09 ± 0.02					0.10 ± 0.01				
[O II]/H β	-					4.74 ± 1.15				
[O III]/H β	0.58 ± 0.10					0.42 ± 0.06				
Line	Neb4c					Neb4d				
	λ_{obs}	F_{obs}	F_{corr}	S/N	RV	λ_{obs}	F_{obs}	F_{corr}	S/N	RV
[O II] 3726	3729.24	71	129	3	256	3729.55	56	96	3	281
[O II] 3729	3732.24	136	248	6	273	3732.12	94	161	5	264
H γ 4341	4344.53	50	65	10	279	4344.49	33	42	9	276
H β 4861	4865.83	100	100	20	276	4865.83	100	100	25	276
[O III] 5007	5011.54	28	26	8	279	5011.48	24	22	8	276
[O I] 6300	6306.77	43	25	16	306	-	-	-	-	-
[N II] 6527	6532.93	17	9	4	259	6533.09	16	9	6	267
[N II] 6548	6553.92	50	27	12	267	6553.87	48	28	16	265
H α 6563	6568.88	535	286	25	276	6568.88	500	286	25	276
[N II] 6584	6589.57	91	49	20	276	6589.58	84	48	33	277
[S II] 6716	6722.79	192	98	33	281	6722.89	87	48	33	286
[S II] 6731	6737.14	134	68	33	280	6737.28	69	38	33	286
$F_{\text{H}\beta}$	2.69					3.90				
$c(\text{H}\beta)$	0.85 ± 0.12					0.76 ± 0.11				
$E(B - V)$	0.60 ± 0.09					0.53 ± 0.08				
[S II]/H α	0.58 ± 0.04					0.30 ± 0.02				
[N II]/H α	0.17 ± 0.02					0.17 ± 0.01				
[O I]/H α	0.09 ± 0.01					-				
[O II]/H β	3.77 ± 0.97					2.58 ± 0.65				
[O III]/H β	0.26 ± 0.04					0.22 ± 0.04				

Line	Neb4e					Neb4f						
	λ_{obs}	F_{obs}	F_{corr}	S/N	RV	λ_{obs}	F_{obs}	F_{corr}	S/N	RV		
[O II] 3726	3729.39	89	129	9	268	3729.40	104	178	7	269		
[O II] 3729	3732.18	146	211	9	269	3732.17	175	299	12	268		
H γ 4341	4344.56	39	46	10	281	4344.58	45	56	10	282		
H β 4861	4865.82	100	100	25	275	4865.82	100	100	25	275		
[O III] 5007	5011.53	28	27	12	279	5011.52	35	33	12	278		
[O I] 6300	-	-	-	-	-	6306.80	36	22	20	307		
[N II] 6527	6533.06	12	8	5	265	6532.74	15	9	7	251		
[N II] 6548	6553.89	25	17	9	266	6553.73	32	18	14	259		
H α 6563	6568.84	419	286	25	274	6568.79	501	287	25	272		
[N II] 6584	6589.60	44	30	20	278	6589.63	32	18	14	279		
[S II] 6716	6722.83	59	39	25	283	6722.81	50	28	25	282		
[S II] 6731	6737.27	43	29	25	286	6737.22	39	21	25	284		
$F_{\text{H}\beta}$		4.68						3.95				
$c(\text{H}\beta)$		0.52 ± 0.11						0.76 ± 0.11				
$E(B - V)$		0.36 ± 0.08						0.53 ± 0.08				
[S II]/H α		0.24 ± 0.02						0.17 ± 0.01				
[N II]/H α		0.10 ± 0.01						0.06 ± 0.01				
[O I]/H α		-						0.08 ± 0.01				
[O II]/H β		3.40 ± 0.51						4.77 ± 0.68				
[O III]/H β		0.27 ± 0.03						0.33 ± 0.04				

Line	Neb5a					Neb5b						
	λ_{obs}	F_{obs}	F_{corr}	S/N	RV	λ_{obs}	F_{obs}	F_{corr}	S/N	RV		
[O II] 3726	3729.42	100	180	3	271	3729.33	167	265	4	263		
[O II] 3729	3732.06	185	332	5	259	3732.13	241	381	5	265		
H γ 4341	4344.55	68	88	6	280	4344.76	52	64	5	295		
H β 4861	4865.83	100	100	11	276	4865.86	100	100	16	278		
[O III] 5007	5011.46	66	62	10	274	5011.54	57	54	9	279		
[O I] 6300	6306.84	67	39	14	309	6306.83	54	36	12	309		
[N II] 6527	6532.94	45	25	12	260	6533.04	55	35	9	264		
[N II] 6548	6553.65	95	52	20	255	6553.72	80	50	14	258		
H α 6563	6568.82	526	286	25	273	6568.81	461	286	25	273		
[N II] 6584	6589.52	107	58	20	274	6589.42	77	47	20	269		
[S II] 6716	6722.84	146	76	33	284	6722.80	115	69	25	282		
[S II] 6731	6737.19	96	50	33	282	6737.16	70	42	25	281		
$F_{\text{H}\beta}$		1.58						1.59				
$c(\text{H}\beta)$		0.83 ± 0.18						0.65 ± 0.14				
$E(B - V)$		0.58 ± 0.13						0.45 ± 0.10				
[S II]/H α		0.44 ± 0.03						0.39 ± 0.03				
[N II]/H α		0.20 ± 0.02						0.17 ± 0.01				
[O I]/H α		0.14 ± 0.02						0.12 ± 0.01				
[O II]/H β		5.11 ± 1.65						6.45 ± 1.70				
[O III]/H β		0.62 ± 0.12						0.54 ± 0.09				

Line	Neb5c					Neb5d						
	λ_{obs}	F_{obs}	F_{corr}	S/N	RV	λ_{obs}	F_{obs}	F_{corr}	S/N	RV		
[O II] 3726	-	-	-	-	-	-	-	-	-	-		
[O II] 3729	-	-	-	-	-	-	-	-	-	-		
H γ 4341	-	-	-	-	-	-	-	-	-	-		
H β 4861	4865.79	100	100	14	273	4865.76	100	100	14	272		
[O III] 5007	5011.44	61	59	8	273	5011.52	47	45	7	278		
[O I] 6300	6306.88	60	45	16	311	6306.88	56	39	16	311		
[N II] 6527	6532.97	35	26	6	261	6532.96	43	29	6	261		
[N II] 6548	6553.61	73	53	14	253	6553.61	79	52	11	253		
H α 6563	6568.82	392	285	25	273	6568.88	432	286	25	276		
[N II] 6584	6589.49	63	46	12	273	6589.54	73	48	16	275		
[S II] 6716	6722.83	92	65	25	283	6722.82	102	66	25	283		
[S II] 6731	6737.16	61	43	20	281	6737.35	76	49	20	289		
$F_{\text{H}\beta}$		1.57						1.52				
$c(\text{H}\beta)$		0.43 ± 0.15						0.56 ± 0.15				
$E(B - V)$		0.30 ± 0.11						0.39 ± 0.11				
[S II]/H α		0.38 ± 0.03						0.40 ± 0.03				
[N II]/H α		0.16 ± 0.02						0.17 ± 0.02				
[O I]/H α		0.16 ± 0.02						0.14 ± 0.01				
[O II]/H β		-						-				
[O III]/H β		0.59 ± 0.11						0.45 ± 0.09				

Line	Neb5e					Neb6a						
	λ_{obs}	F_{obs}	F_{corr}	S/N	RV	λ_{obs}	F_{obs}	F_{corr}	S/N	RV		
[O II] 3726	3729.48	79	147	4	275	-	-	-	-	-		
[O II] 3729	3732.15	85	159	4	266	-	-	-	-	-		
H γ 4341	4344.58	46	61	7	282	-	-	-	-	-		
H β 4861	4865.83	100	100	25	276	4865.86	100	100	5	278		
[O III] 5007	5011.61	17	16	4	283	-	-	-	-	-		
[O I] 6300	6306.81	40	23	10	308	6306.84	28	26	7	309		
[N II] 6527	6533.23	23	12	6	273	-	-	-	-	-		
[N II] 6548	6553.81	58	31	16	262	6553.75	30	28	7	260		
H α 6563	6568.85	548	287	25	274	6568.85	310	286	25	275		
[N II] 6584	6589.46	83	43	20	271	6589.55	39	36	25	276		
[S II] 6716	6722.78	139	70	33	281	6722.86	54	49	25	285		
[S II] 6731	6737.17	103	51	33	281	6737.17	38	35	25	282		
$F_{\text{H}\beta}$		2.48						3.45				
$c(\text{H}\beta)$		0.88 ± 0.11						$0.11^{+0.34}_{-0.11}$				
$E(B - V)$		0.62 ± 0.08						$0.08^{+0.24}_{-0.08}$				
[S II]/H α		0.42 ± 0.03						0.29 ± 0.02				
[N II]/H α		0.15 ± 0.01						0.12 ± 0.01				
[O I]/H α		0.08 ± 0.01						0.09 ± 0.02				
[O II]/H β		3.06 ± 0.86						-				
[O III]/H β		0.16 ± 0.04						-				

Line	λ_{obs}	Neb6b				Neb6c				
		F_{obs}	F_{corr}	S/N	RV	λ_{obs}	F_{obs}	F_{corr}	S/N	RV
[O II] 3726	-	-	-	-	-	-	-	-	-	-
[O II] 3729	-	-	-	-	-	-	-	-	-	-
H γ 4341	-	-	-	-	-	-	-	-	-	-
H β 4861	4865.78	100	100	5	273	4865.88	100	100	5	279
[O III] 5007	5011.42	100	98	5	272	-	-	-	-	-
[O I] 6300	6306.85	30	26	8	310	6306.94	39	28	7	314
[N II] 6527	6532.86	21	18	4	256	-	-	-	-	-
[N II] 6548	6553.67	30	25	5	256	6553.65	35	23	11	255
H α 6563	6568.84	341	286	25	274	6568.84	424	285	25	274
[N II] 6584	6589.84	43	36	14	289	6589.50	62	41	20	273
[S II] 6716	6722.91	53	44	20	287	6722.78	67	44	25	281
[S II] 6731	6737.20	36	30	12	283	6737.20	55	36	25	283
$F_{\text{H}\beta}$		3.61					2.64			
$c(\text{H}\beta)$		$0.24^{+0.31}_{-0.24}$					0.54 ± 0.34			
$E(B - V)$		$0.17^{+0.21}_{-0.17}$					0.37 ± 0.24			
[S II]/H α		0.26 ± 0.03					0.28 ± 0.02			
[N II]/H α		0.12 ± 0.01					0.14 ± 0.01			
[O I]/H α		0.09 ± 0.01					0.10 ± 0.02			
[O II]/H β		-					-			
[O III]/H β		0.98 ± 0.33					-			

Line	λ_{obs}	Neb6d			
		F_{obs}	F_{corr}	S/N	RV
[O II] 3726	-	-	-	-	-
[O II] 3729	-	-	-	-	-
H γ 4341	-	-	-	-	-
H β 4861	4865.88	100	100	5	279
[O III] 5007	-	-	-	-	-
[O I] 6300	6306.83	31	25	7	309
[N II] 6527	6532.98	17	13	5	262
[N II] 6548	6553.80	36	27	11	262
H α 6563	6568.90	379	287	25	277
[N II] 6584	6589.45	64	48	20	271
[S II] 6716	6722.86	79	59	25	285
[S II] 6731	6737.15	53	39	25	281
$F_{\text{H}\beta}$		3.19			
$c(\text{H}\beta)$		0.38 ± 0.34			
$E(B - V)$		0.27 ± 0.24			
[S II]/H α		0.34 ± 0.03			
[N II]/H α		0.17 ± 0.02			
[O I]/H α		0.09 ± 0.02			
[O II]/H β		-			
[O III]/H β		-			

Appendix C: Disentangling the origin of the nebular emission

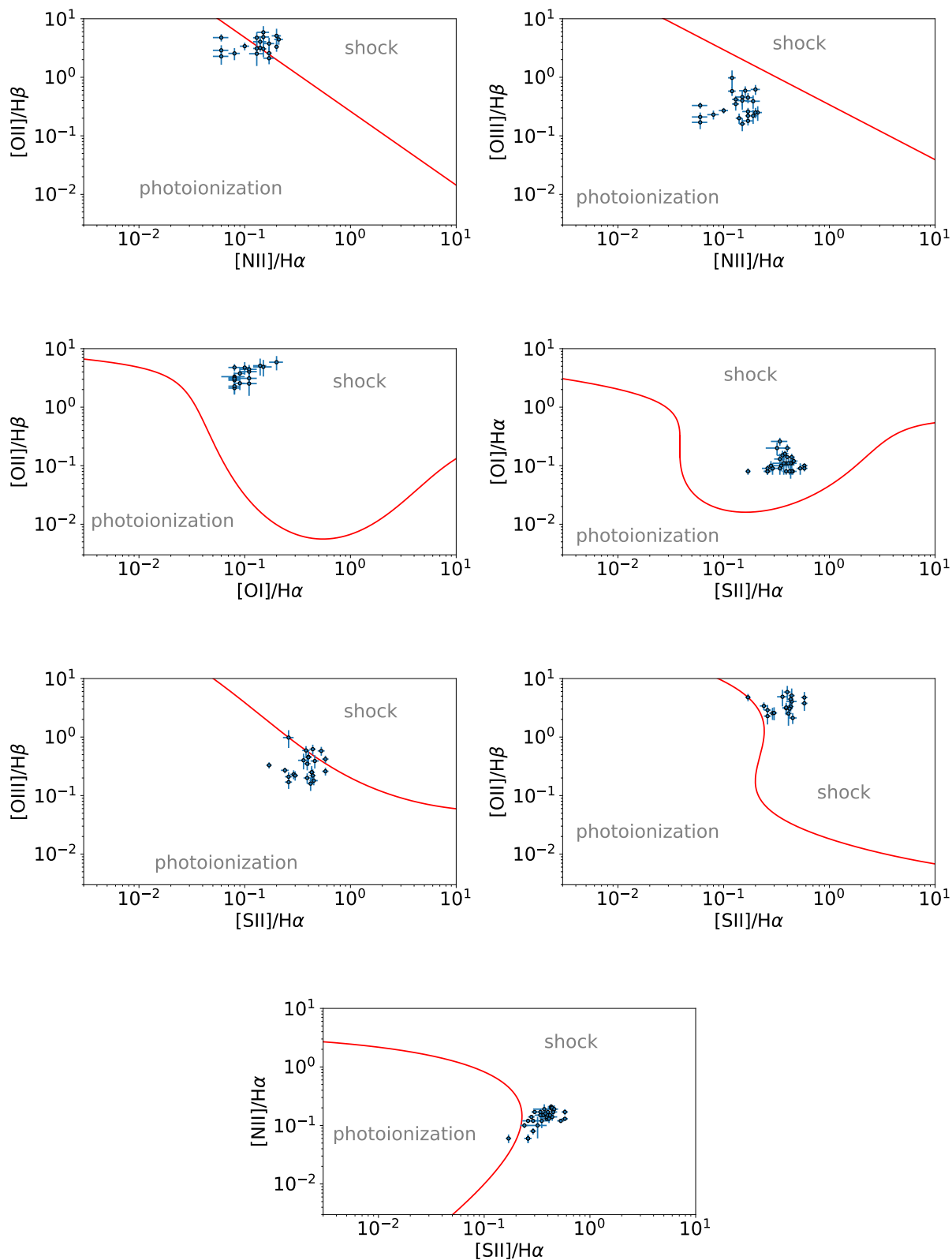


Fig. C.1: Diagnostic plots comparing the line ratio measurements (blue dots) in the CSM around [W60] B90 with the theoretical predictions of shocked vs. photoionized emission (red line, Kopsacheili et al. 2020).

Appendix D: Spectroscopic analysis of the B-star near [W60] B90

Apart from the long-slit spectroscopy observations presented in Table 1, we placed the slit in another position that was finally excluded from the analysis of [W60] B90 and the shocked material. The slit was centered at the coordinates RA=05:24:18.38 Dec=-69:38:54.9 on the star with *Gaia* DR3 ID 4657970853790677248 (Fig. D.1). The data was obtained on the same night as Epoch4 and Neb6, under the same technical settings, and reduced following the procedure described in Sect 2.2.

We analyze the spectral region 3900 – 4800Å (see Fig. D.2) using the criteria of Walborn & Fitzpatrick (1990) to determine the spectral classification of the star. The absence of He II lines and the presence of He I lines indicate a B spectral type. More specifically, the absence of He II $\lambda 4686$ suggests a type later than B0.7, while the absence of Si II lines $\lambda\lambda 4128 - 4130$ supports a type not later than B2. The weak presence of C III+O II blends $\lambda\lambda 4070$ and 4650 suggests a B1 spectral type. The main criterion for the luminosity classification in B1 stars is the weakness of Si III $\lambda 4552$ compared to He I $\lambda 4387$, which suggests a V luminosity class. This classification is also supported by the low intensity of the Si IV $\lambda 4089$ line compared to He I lines $\lambda\lambda 4026$ and 4121, as well as the low ratio of Si IV $\lambda 4116$ /He I $\lambda 4121$. We therefore report a B1V spectral classification for this star. Furthermore, the feature in the right wing of H γ and the RV inconsistency in the He I $\lambda 6678$ line hint at a low luminosity companion, but further investigation is needed to confirm it. Finally, we find a $P_{LMC}=0.99$ (see Sect. 3.1; Jiménez-Arranz et al. 2023) and a radial velocity of 266 ± 7 km s $^{-1}$ from the Balmer series, therefore confirming its membership to the LMC.

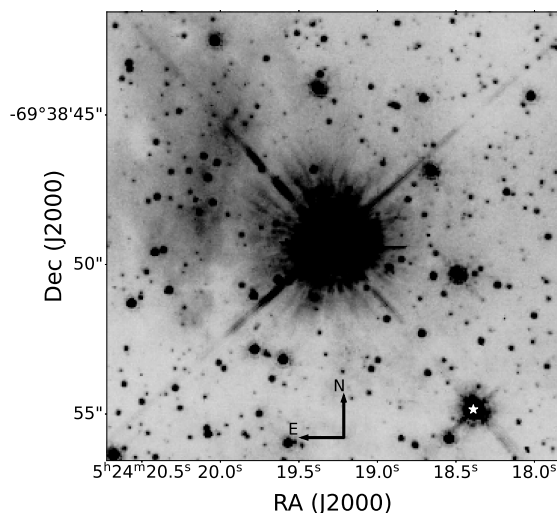


Fig. D.1: *HST* F675W image showing the location of [W60] B90 and the B-star, marked with a star symbol.

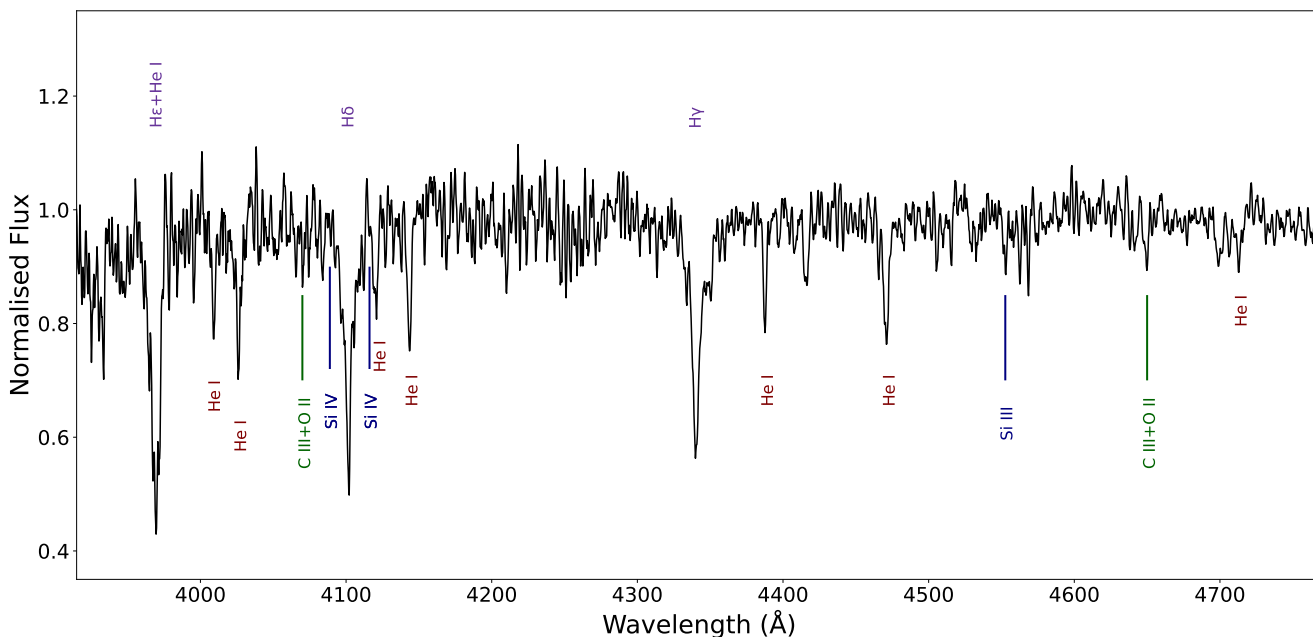


Fig. D.2: Spectral region showing the lines used to determine the B1V spectral type of the star.